Time-resolved and Doppler-reduced Laser Spectroscopy on Atoms

Håkan Bergström

TEKNISKA HÖGSKOLAN I LUND
INSTITUTIONEN FÖR FYSIK

LUND INSTITUTE OF TECHNOLOGY
DEPARTMENT OF PHYSICS

Time-resolved and Doppler-reduced Laser Spectroscopy on Atoms

Håkan Bergström

AKADEMISK AVHANDLING

som för avläggande av teknologie doktorsexamen vid tekniska fakulteten vid Lunds Universitet kommer att offentligen försvaras vid
Institutionen för Fysik, Sölvegatan 14, Hörsal B,
fredagen den 8:e november 1991, kl 13:15.

Organization
LUND UNIVERSITY

Department of Physics
Lund Institute of Technology
P.O.Box 118, S-221 00 LUND, SWEDEN

Document name
DOCTORAL DISSERTATION

Date of issue
OKTOBER 1991

CODEN:
LUTFD2/(TFAF-1019)/1-53/(1991)

Author(s)
Håkan Bergström

Sponsoring organization

Title and subtitle

Time-resolved and Doppler-reduced Laser Spectroscopy on Atoms

Abstract

Radiative lifetimes have been studied in neutral boron, carbon, silicon and strontium, in singly ionized gadolinium and tantalum and in molecular carbon monoxide and C_2. The time-resolved techniques were based either on pulsed lasers or pulse-modulated CW lasers. Several techniques have been utilized for the production of free atoms and ions such as evaporation into an atomic beam, sputtering in hollow cathodes and laser-produced plasmas.

Hyperfine interactions in boron, copper and strontium have been examined using quantum beat spectroscopy, saturation spectroscopy and collimated atomic beam spectroscopy.

Measurement techniques based on effusive hollow cathodes as well as laser produced plasmas in atomic physics have been developed.

Investigations on laser produced plasmas using two colour beam deflection tomography for determination of electron densities have been performed.

Finally, new possibilities for view-time-expansion in light-in-flight holography using mode-locked CW lasers have been demonstrated.

Key words
Radiative lifetime, hyperfine structure, hollow cathode, laser produced plasma, boron, carbon, silicon, strontium, aluminum, copper, tantalum, gadolinium, C_2, CO.

Classification system and/or index terms (if any)
PACS: 32.70, 35.10, 35.80

Supplementary bibliographical information

Language
English

ISSN and key title

ISBN

Recipient's notes

Number of pages
164

Price

Security classification

Distributed by (name and address)

I, the undersigned, being the copyright owner of the abstract of the above-mentioned dissertation, hereby grant to all reference sources permission to publish and disseminate the abstract of the above-mentioned dissertation.

Signature: Håkan Bergström

Date: Oktober 15, 1991

Time-resolved and Doppler-reduced Laser Spectroscopy on Atoms.

Håkan Bergström

Department of Physics
Lund Institute of Technology
1991

Lund Reports on Atomic Physics
LRAP-125 (LUTFD2-TFAF-101R-1-53-1991)

Till Mor och Far

CONTENTS

Abstract

Radiative lifetimes have been studied in neutral boron, carbon, silicon and strontium, in singly ionized gadolinium and tantalum and in molecular carbon monoxide and C_2. The time-resolved techniques were based either on pulsed lasers or pulse-modulated CW lasers. Several techniques have been utilized for the production of free atoms and ions such as evaporation into an atomic beam, sputtering in hollow cathodes and laser-produced plasmas.

Hyperfine interactions in boron, copper and strontium have been examined using quantum beat spectroscopy, saturation spectroscopy and collimated atomic beam spectroscopy.

Measurement techniques based on effusive hollow cathodes as well as laser produced plasmas in atomic physics have been developed.

Investigations on laser produced plasmas using two colour beam deflection tomography for determination of electron densities have been performed.

Finally, new possibilities for view-time-expansion in light-in-flight holography using mode-locked CW lasers have been demonstrated.

List of papers

1. H. Bergström, C. Levinson, H. Lundberg, S. Svanberg, C.G. Wahlström and Zhao You Yuan, Hyperfine-dependent lifetimes induced by singlet-triplet mixing. Phys.Rev. A33, 2387 (1986).

2. H. Bergström, C. Levinson and H. Lundberg, Natural radiative lifetimes in the 5snd ^{1}D series of Sr I. Z.Phys.D (Atoms Molecules and Clusters) 2, 127 (1985).

3. H. Bergström, H. Lundberg, A. Persson, W. Schade and Zhao You Yuan, Lifetime measurements in Ta II using a pulsed discharge. Phys.Scr. 33, 513 (1986).

4. H. Bergström, E. Biemont, H. Lundberg and A. Persson, Transition probabilities for Gd II and a new determination of the solar abundance of gadolinium. Astron.Astrophys. 192, 335 (1988).

5. H. Bergström, G.W. Faris, H. Hallstadius, H. Lundberg and A. Persson, Investigations of radiative lifetimes in the 3p5p configuration of neutral silicon. Z.Phys.D (Atoms Molecules and Clusters) 13, 29 (1989).

6. H. Bergström, G.W. Faris, H. Hallstadius, H. Lundberg, A. Persson and C.G. Wahlström, Radiative lifetimes and hyperfine-structure studies on laser-evaporated boron. Z.Phys.D (Atoms Molecules and Clusters) 8, 17 (1988).

7. H. Bergström, W.X. Peng and A. Persson, Two different types of hollow-cathode discharges used for high resolution laser spectroscopy on copper. Z.Phys.D (Atoms Molecules and Clusters) 13, 203 (1989).

8. A. Persson and H. Bergström, SIGAV, a program for signal averaging and evaluation in high-resolution laser spectroscopy experiments. Lund Reports on Atomic Physics, LRAP-98 (1989).

9. H. Bergström, H. Hallstadius, H. Lundberg and A. Persson, Detection of carbon using amplified laser-induced fluorescence. Chem.Phys.Lett. 155, 27 (1989).

10. H. Bergström, H. Lundberg and A. Persson, Investigations of stimulated emission on B-A lines in CO. Accepted for publication in Z.Phys.D (Atoms Molecules and Clusters).

11. G.W. Faris and H. Bergström, Two-wavelength beam-deflection technique for electron density measurements in laser-produced plasmas. Appl.Opt. 30, 2212 (1991).

12. N. Abramson, S.G. Pettersson and H. Bergström, Light-in-flight recording. 5: Theory of slowing down the faster-than-light motion of the light shutter. Appl.Opt. 28, 759 (1989).

13. N. Abramson, S.G. Pettersson and H. Bergström, Light-in-flight recording. 6: Experiment with view-time expansion using a skew reference wave. Appl.Opt. 28, 766 (1989).

Introduction.

The word *atom* was introduced by the Greek natural philosopher Democrites around 400 B.C. The word atom (the indivisible) means a component of matter which cannot be further divided without loosing it's characteristics. Early in the 19'th century the physicists showed that matter is build from atoms, which were then arranged in the periodic system by Mendeleev. In 1833 Faraday discovered the atomism of electricity. When Planck in the year 1900 assumed that energy was only allowed to change discretely (atomised by so called light quanta or photons) the quantum theory was born. During the period from 1910 to 1930 Rutherford, Einstein, Bohr, Sommerfeld, Born, Heisenberg, Schrödinger, Pauli, Dirac and others developed the quantum theory which now is considered to be one of the most accurate theories ever devised.

The most important tool for an experimentalist in physics today is the laser. The first laser was constructed by T.H. Maiman in 1960. It was a flash- lamp pumped ruby laser with a pulse duration of 1 ms. The discovery of laser action in organic dyes (in 1966 by P.P. Sorokin *et al*) and the introduction of wavelength-selective elements (in 1970 by O.G. Peterson *et al*) inside the laser resonator made it possible to obtain tunable narrow-band radiation over a large spectral range [2.33]. Recent developments of laser technology have opened up an enormous amount of possibilities not only in the atomic physics area. Nowadays lasers are capable of delivering pulse powers in the terawatt range, pulse durations of a few femtoseconds or linewidths below 1 Hz.

The quest for an experimentalist in atomic physics is to investigate the interaction between atoms and radiation and thereby gain more accurate information on the structure of electronic states which is needed to test the validity of existing theories. Furthermore, there is a need to develope new tools and techniques for the determination of structures or quantities which have so far been impossible to measure in a laboratory.

The pursuit of knowledge is motivated by the curiosity to reveal the secrets of nature. Also, researchers in astrophysics, plasma physics, chemical physics as well as in more applied areas like environmental control and energy production demand more and better atomic, ionic and molecular data.

Although the title "Time-resolved and doppler-reduced laser spectroscopy" does not include the work in all papers, I consider that the most

important parts of the experimental studies are covered with this. Regarding atoms the discussions in the following apply to ions and molecules as well. Radiative properties have been examined in the following atoms: B, C, Si, Sr, Al and Cu, the ions investigated are: TaII, GdII and BII and, finally the molecules: C_2 and CO.

The outline of the thesis is a brief description of the underlaying atomic theory required for the discussion of the performed experiments. The main subject treats the difficulties in producing free atoms and ions to allow determination of natural radiative decay rates, i.e., unaffected by collisions, magnetic or electric fields and other environmental perturbations. These experiments have led to the development of some experimental techniques that are compared with previously existing techniques. Finally, the analysis of the experimental data is discussed together with different sources of error related to the specific techniques used.

1. Theory

1.1. Energy-levels

The atomic energy levels are determined by the energy eigenvalues of the time-independent Schrödinger equation

$$H \Psi_n = E_n \Psi_n, \qquad (1.1)$$

where the index n denotes different electronic states. The energy operator H is normally described by the following sum of terms, each representing a particular type of force acting on the i:th electron of the atom:

$$H = \sum [H_{kin} + H_{C+} + H_{C-} + H_{so} + H_{hfs} + H_m + H_e + (H_{iso})] \qquad (1.2)$$

Where the summation is over all i electrons. This is sometimes referred to as the non-relativistic Hamiltonian even though some of the interactions of magnetic nature (due to the intrinsic spin of the electron as well as the nuclei) have large relativistic contributions. We will now discuss the different terms of the Hamiltonian separately.

The first three terms are the dominating contributors to the energy of the atom and thus determine the gross structure of the energy level diagram (figure 1a). These can be written as:

$$H_{kin.} + H_{C+} + H_{C-} = p_i^2/2m - Ze^2/4\pi\varepsilon_0 r_i + \sum_{j<i} (e^2/4\pi\varepsilon_0 |r_i - r_j|) \qquad (1.3)$$

and describe the kinetic energy due to the motion of the electrons, the energy due to the attractive electrostatic Coulomb force from the nucleus and the repulsive electrostatic Coulomb force from the other electrons acting on the i:th electron.

The fourth term is the spin-orbit interaction which causes a splitting of energy levels indicated in figure 1b (fine structure). The orbital motion of the other electrons as well as that of the nucleus give rise to a magnetic field in the reference system of the i:th electron. This magnetic field will interact with the intrinsic spin of the electron. In a central potential field u this can be expressed as

$$H_{so} = \alpha^2/2 \cdot \langle 1/r \cdot \partial u/\partial r \rangle \cdot \mathbf{l} \cdot \mathbf{s} = \xi \cdot \mathbf{l} \cdot \mathbf{s} \qquad (1.4)$$

where $\mathbf{l}$ and $\mathbf{s}$ are the angular momentum ($\mathbf{r} \times \mathbf{p}$) and the spin (angular momentum) operators.

The fifth term is normally divided into more terms. These terms are components of a multipole expansion of the electron-nucleus electronic interaction with the first dominating term being the Coulomb attraction (H_{C+}), and the second and third terms describing the magnetic-dipole and the electric-quadrupole interaction. The interactions described by H_{hfs} give rise to the so called hyperfine structure of the energy levels.

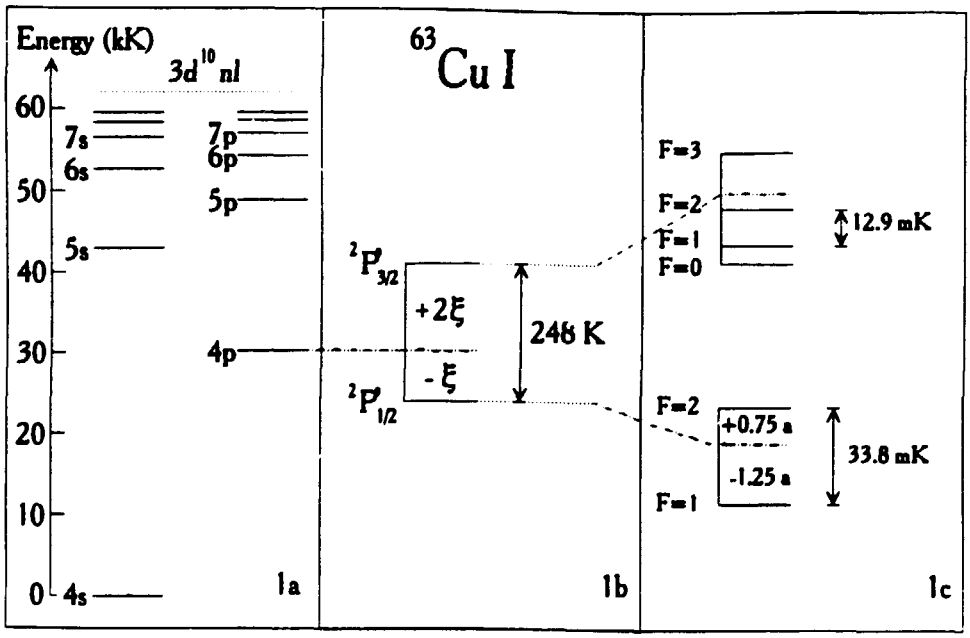

Figure 1. Schematic energy level diagram of Cu. a) shows the gross energy determined by the kinetic energy term and the Coloumb terms for the electron configuration: $1s^2 2s^2 2p^6 3s^2 3p^2 3d^{10} nl$. b) shows the spin orbit splitting of the 4p state. c) shows the splitting of the two fine-structure levels $^2P^o_{1/2}$ and $^2P^o_{3/2}$ into hyperfine-structure levels due to the nuclear spin.

The multipole expansion of the vector potential arising from electric and magnetic properties of the nucleus has great advantages. The coefficients in the multipole expansion can be described by spherical tensors of rank 1 (e.g. Y_{LM}) which gives rise to useful orthogonality relations with respect to angular integrations (see, e.g., Brink and Satchler [1.1]).

According to Weissbluth [1.2] H_{hfs} can be written as

$$H_{hfs} = H_{magn} + H_{el} \qquad (1.5)$$

with

$$H_{magn} = 2g_I\beta^2(\mu_0/4\pi)\cdot[l_i/r_i^3 - s_i/r^3 + 3(s_i\cdot r_i)r_i/r_i^5 + (8\pi/3)\delta(r_i)s_i]\cdot I \qquad (1.6)$$

It may be of interest to note that the vector field resulting from the electrons at the nucleus (r=0) can be described by tensor operators (or angular momentum operators) which in turn can be combined with the nuclei multipole tensors (normally by generalized scalar products) into spherical tensors. The second and third terms in the bracket of the magnetic-dipole term is then the contribution from the electronic rank-1 tensor $(sC^2)^1$ discussed below.

The first term is associated with the orbital motion and the second and third terms are due to the spin of the electrons; all these terms vanish for s electrons. The last term is the so called Fermi contact term which gives a non-zero contribution for s electrons only, since the δ function maps the electronic wavefunction at the nucleus under radial integration, i.e., the interaction is proportional to $|\Psi(0)|^2$. However, since the electrons interact with each other e.g. by spin-spin interaction, non-s electrons will interact with the two s electrons in a closed s-subshell and affect the electron with parallel and anti-parallel spin differently. This will in turn result in unequal probability for the two s electrons being at the nucleus (r=0), an effect referred to as spin polarization.

The generalized description with nuclear multipole tensors $\mathbf{M}^k$, where k represents a 2^k-pole, and Coulomb-interaction tensor-operators $\mathbf{C}^k$ (renormalized spherical harmonic) formed by coupling of the spin and orbital vector-operators has been used by Lindgren and Rosén [1.3]. In this description the electric quadrupole interaction (using atomic units) can then be written as

$$\mathbf{H}_{el} = -\frac{1}{2}\sum \mathbf{C}_i^2 \cdot \mathbf{Q}^2 r^{-3} \qquad (1.7)$$

which may be identified as the second term in the expansion $\mathbf{H}_{hfs} = \sum_{k=1}^{\infty} \mathbf{C}_i^k \cdot^{(k)} \mathbf{M}^k$. The symbol $\cdot^{(k)}$ denotes a generalized dot product (scalar product).

The Hamiltonian can normally be greatly simplified. For instance, when investigating hyperfine spectra only two constants, the a and b factor, are sufficient to describe the structure. The analysis of experimental spectra which is the main subject of this thesis will be discussed in section 2.4.

The Zeeman effect is due to an interaction between the magnetic moments of the electrons and the nuclei and an external B-field and is described by

$$\mathbf{H}_{magn} = -(\bar{\mu}_J + \bar{\mu}_I)\cdot \mathbf{B} \qquad (1.8)$$

It is extremely important to be able to control external magnetic fields in order not to affect e.g. lifetime measurements. This will be discussed later.

The term in the expansion is due to the interaction between a static external electric field the electric dipole moment of the atom, which can be represented as

$$\mathbf{H}_{el} \propto \mathbf{D}_i \cdot \mathbf{E}_{el} \qquad (1.9)$$

and is referred to as the Stark effect.

The last term $\mathbf{H}_{iso}$ is normally not introduced in the Hamiltonian since the

isotope shift is not due to interactions within an atom but rather an effect of differences between isotopes. The energy levels of two isotopes will differ due to their different mass, volume and shape of the nuclei. Isotopic shifts may be separated into the normal mass-shift, the specific mass-shift and the volume isotope-shift.

When all interactions of interest are included in the Hamiltonian we are ready to calculate the energies of the different electronic states as well as the wavefunctions Ψ_n. This will however demand immense computational powers. The normal solution is to calculate wavefunctions using only the first three terms. With these wavefunctions the relevant interactionHamiltonian, e.g. the one describing the hyperfine interaction H_{hfs}, is treated using perturbation theory. This can be done with a number of different methods and the one used in this work is the Multi-Configuration Hartree-Fock (MCHF) approach [1.4]. This method is briefly outlined below.

1.2 Calculation of energy levels

The atomic wavefunction of an atom with N electrons used in the Hartree Fock method, is an antisymmetric product of N one-electron spin-orbitals. These wavefunctions are referred to as Slater determinants. Each orbital has a unique set of quantum numbers all of which must be different.

The reason for choosing antisymmetric wavefunctions is that the electrons are Fermions (i.e. spin-1/2 particles). The wave functions are chosen to be orthogonal and normalized or expanded in a set of basis functions, which in turn are normalized and orthogonal. If these wave functions are inserted into the Schrödinger equation we can calculate the energy eigenvalue of a specific state as the expectation value of the Hamiltonian. Using the Dirac Bra-Ket notation for the wave function $|\Psi>$ this can be written as

$$E_n = <\Psi|H_n|\Psi> \qquad (1.10)$$

A gross energy value is calculated using the less complicated Hartree-Fock (HF) operator, a Hamiltonian with only one- and two-electron operators

$$H_{kin.} + H_{C+} + H_{C-}. \qquad (1.11)$$

The last Coulomb-repulsion term is in turn described by two terms for convenience. The term resulting in the potential from all electrons is called the direct term and the second so called exchange term has to be subtracted so that the interaction on the i'th electron on itself is avoided.

By diagonalizing the energy matrix (the expectation value of the Hamiltonian) we obtain the energy eigen-values as the diagonal elements and the wavefunctions as the columns of the transformation matrix. The basis set chosen to represent the atom is the one giving the lowest energy in some iterative routine. Since the HF equation is dependent on the wavefunction we have to start out with some arbitrary wavefunction. If the solutions to this HF equation can be used as new wave functions which finally end up being the same as the input wavefunctions, the aim has been achieved. In this case the solution is said to be self-consistent. This is why the Hartree-Fock method is called a Self Consistent Field method. The "Multi Configurations" are due to the choice of a superposition of many different configurations weighted together to describe each single state. These weights may be obtained e.g. by varying the radial parts of the configurations with the energy fixed.

1.3 Radiative properties

Until now we have discussed static properties of the atoms. If the atom is irradiated e.g. by laser or black-body radiation, the photons will interact with the atom. This interaction can be treated in many different ways. One is to incorporate the vector potential **A** of the radiation field in the Hamiltonian by substituting $\mathbf{p}_i$ (in the term $H^1_{kin.}$) by [1.2]

$$\mathbf{p}_i \rightarrow \mathbf{p}_i - e\mathbf{A}/c \qquad (1.12)$$

Another method is to use the so called density matrix formalism [1.5], which is based on the time-dependent Schrödinger equation

$$H \cdot \Psi(r,t) = i\hbar \cdot \partial\Psi(r,t)/\partial t \qquad (1.13)$$

A density matrix operator is introduced as $\rho = |\Psi><\Psi|$. This corresponds to an ensemble average over the ket and bra state vectors of the wavefunction Ψ. $\Psi(r,t)$ is normally expanded in some basis set of orthogonal base functions $u_k(r)$, e.g.

$$\Psi(r,t) = \sum_k c_k(t)u_k(r). \qquad (1.14)$$

If the density matrix is described by its matrix elements

$$\rho_{nm} = <n|\rho|m> = \overline{c_n c_m^*} \qquad (1.15)$$

we get, after some manipulation, the equation of motion for ρ,

$$\partial\rho/\partial t = 1/i\hbar \cdot [H,\rho], \qquad (1.16)$$

which is known as the Liouville equation.

In this equation the Hamiltonian is written as $H = H_0 + H_{int}$ where H_0 may be the Hamiltonian discussed in section 1.1. The radiative properties can now be dealt with using the interaction Hamiltonian

$H_{int} = -er \cdot E$ (1.17)

which describes the interaction with radiation in the electric dipole approximation. In this picture the eigen energies E_k are given by

$H_0|k> = E_k|k>$. (1.18)

The matrix elements ρ_{nn} corresponds to the population in the state $|n>$ and the off diagonal element ρ_{nm} is the portion of coherent admixture between the two states $|n>$ and $|m>$.

The methods mentioned above are normally too complex to use and thus demand immense computer power to perform calculations when macroscopic processes come into play. An example of this could be the calculation of the resulting stimulated emission (SE) after two-photon excitation. Instead a simple conceptual model for such calculations, including the dynamics of e.g. an atom, could be the rate equation method. This technique was used in paper 9 and 10 and will later be discussed in detail.

In the experiments laser excitation has been used extensively for preparing the atoms in excited states. The process has not been studied very much, except for the determination of two-photon absorption rates. Most of the papers have been concerned with the measurements of lifetimes, or spontaneous transition rates, hereafter denoted A factors. Furthermore, we have examined other dynamic properties such as multiple scattering, quenching and ionization and how these processes can interfere in the determination of A factors.

The theory needed to describe the spontaneous decay time of excited atoms is quite simple. The atom will stay in the excited state $|e>$ for some time and after a while decay spontaneously to some final state $|f>$ according to a Poissonian distribution.

$\partial N_e/\partial t = -N_e \sum A_{ef}$ (sum over final states f) (1.19)

i.e., the number of emitted photons from an excited ensemble of atoms will follow the common exponential decay law

$N_e(t) = N(t_0) \cdot \exp[(t_0-t)/\tau_e]$. (1.20)

The lifetime τ is related to the A factor as well as to other radiative quantities of the atom. Some of the relations which can be found in [1.2] or [1.6] will be presented here since they are used later in the text.

The lifetime is calculated as the inverse of the sum of all A_{ef} factors from a specific excited state $|e>$.

$1/\tau_e = A_e = \sum A_{ef}$ (sum over f) (1.21)

The A_{ef} factor for a transition from $|e>$ to $|f>$ can in turn be calculated

from the wavefunctions of the two states involved (using the electric dipole approximation, neglecting the degeneracy of the levels) using the so called length form

$$A_{ef} = \frac{4\pi^2 \cdot e^2}{3\varepsilon_0 h} g_f \lambda^{-3} |\langle \Psi_e | \bar{r} | \Psi_f \rangle|^2 \quad (1.22)$$

The A factor is also connected to the one-photon absorption coefficient (the Einstein B factor) as

$$A_{ef} = 8\pi h \lambda^{-3} \cdot \frac{g_f}{g_e} \cdot B_{fe} \quad (1.23)$$

B_{fe} is in turn the same as the stimulated emission coefficient B_{ef} except for the statistical weight factors g_e and g_f

$$B_{ef} \cdot g_e = B_{fe} \cdot g_f \quad (1.24)$$

Now, if we examine a two-level atom with a ground state $|g\rangle$ and an excited state $|e\rangle$, the processes discussed so far can be accounted for in a rate equation system. It should be noted that the rate of excitation W_{ge} is proportional to the spectral energy density of the laser $\rho_L(\nu)$ as

$$W_{ge} = B_{ge} \cdot \rho_L = B_{ge} \cdot I_L / c. \quad (1.25)$$

The unit of the spectral density $I_L(\nu)$ of the laser intensity is [Watt·s/·m^2]. The rate equation system for this simplified atom becomes

$$\partial N_e / \partial t = B_{eg} \cdot \rho_L [N_g \cdot (g_e/g_g) - N_e] - A_{eg} N_e \quad (1.26)$$

$$\partial N_g / \partial t = -B_{eg} \cdot \rho_L [N_g \cdot (g_e/g_g) - N_e] + A_{eg} N_e \quad (1.27)$$

It is clear that $N_e + N_g$ must be constant which indeed is fulfilled by the equations since the population changes in the two states balance exactly.

It is not difficult to include more levels or to introduce other processes, as ionization, quenching and multi-photon excitation in the analysis. To discuss how the atomic line profiles or the laser bandwidth come into play we first take a brief look at the different broadening mechanisms for the atoms.

Due to the finite lifetime of the excited state, the Heisenberg uncertainty principle imposes an energy width, which is often referred to as the natural linewidth. Neglecting other broadening mechanisms, the line profile corresponds to the Lorentzian absorption cross-section

$$\sigma(\omega) = \frac{\gamma}{(\omega - \omega_0)^2 + (\gamma/2)^2} \quad (1.27)$$

with a full width at half maximum of

$$\Delta\omega_{fwhm} = \gamma_e + \gamma_f = 1/\tau_e + 1/\tau_f \quad (1.28)$$

The peak frequency ω_0 corresponds to the atomic transition frequency. Normally the final state is the ground state and the width due to the final state lifetime will then disappear ($\gamma_f = 0$). Due to the recoil of the

atom when the photon is emitted, there will be a shift which is normally to small to be resolved.

Collision processes can be included as a correction of the lifetime

$$\gamma' = 1/\tau_e + Q_e \cdot p \qquad (1.29)$$

where Q_e [/s·mbar] is the quenching cross section and p [mbar] the pressure.

If we want to examine the pressure broadening (referred to as homogeneous broadening mechanisms since all atoms are equally affected) we must distinguish between the elastic and inelastic collisions.

The quenching process is due to inelastic collisions and gives rise to a broadening γ_b^{inel}. It is of great importance to have this process under control since it may influence a lifetime or number density measurement.

The elastic collisions change the phase of the atoms, which gives rise to a shift ω_s^{el} as well as an additional broadening γ_b^{el}. The resulting line profile can then be written

$$\sigma(\omega) = \frac{\gamma + \gamma_b^{el} + \gamma_b^{inel}}{(\omega-\omega_0-\omega_s^{el})^2+([\gamma_b^{el} + \gamma_b^{inel} + \gamma]/2)^2} \qquad (1.30)$$

The major contribution to the spectral linewidth is normally the inhomogeneous broadening due to the motion of the atoms.

The Doppler shift changes the absorption frequency to $\omega = \omega_0(1 \mp v_{\parallel}/c)$ which must be taken into the absorption lineprofile. The absorption cross-section can be modified to account for the Doppler shifts if we neglect collisions for a while and replace $\omega-\omega_0$ in $\sigma(\omega)$ by $\omega-\omega_0-kv\cos\varphi$ where $\cos\varphi$ come from the dot product $\mathbf{k}\cdot\mathbf{v}$ of the excitation wave vector and the atomic velocity vector (only the parallel velocity component gives rise to the Doppler shift).

$$\sigma(\omega) = \frac{\gamma}{(\omega-\omega_0-kv\sin\varphi)^2+(\gamma/2)^2} \qquad (1.31)$$

If we write the velocity distribution of the atoms as W(v) the resulting line profile can be obtained by integrating the product of the line profile $\sigma(\omega)$ and the velocity distribution W(v) over all velocities.

If the motion is the thermal motion of the atoms (e.g. a gas in a cell at thermal equilibrium) the velocity distribution will follow a Maxwellian distribution (this will be discussed in section 2.2.1). Neglecting the homogeneous broadening, we use the fluorescence intensity I(ω) to describe an inhomogeneously broadened Gaussian line profile.

$$I(\omega) = \frac{1}{\Delta\omega_D\sqrt{\pi}} \exp\left[-\left[\frac{\omega-\omega_0}{\Delta\omega_D}\right]^2\right] \qquad (1.32)$$

$\Delta\omega_D = \omega_0 v_p/c$ is the 1/e Doppler width and $v_p = \sqrt{2kT/M}$ the most probable velocity. In this case the full width at half maximum corresponds to

$$\Delta\omega_{fwhm} = 7.16 \cdot 10^{-7} \cdot \omega_0 \sqrt{T/M}, \qquad (1.33)$$

where T is the temperature and M the atomic mole weight.

Normally we have to take both homogeneous and inhomogeneous broadening into account which will lead to a so called Voigt profile. The Voigt profile is obtained by convolving the Lorentzian line profile with the Gaussian line profile.

When the atoms are probed by the laser, the resulting absorption profile may be different from the line profiles discussed above. Normally, the laser line width is either much more narrow, which is the case with a continuous wave single-mode laser (used when probing hyperfine structures in the spectral domain), or much broader, which is sometimes the case with pulsed lasers (e.g. used in "single shot" measurements of lifetimes or when measuring hyperfine structures in the time domain). In the first case we may neglect the laser profile, however, it may be noted that it has normally a Lorentzian line profile with $\Delta\nu_{fwhm} \approx 1$ MHz.

If the transition is saturated, i.e., there is such a high laser intensity that the induced transition rate becomes equal to or larger than the total decay rate, the line profile will broaden. This can sometimes be accounted for [1.6] by substituting γ in $\sigma(\omega)$ by

$$\gamma_S = \gamma \sqrt{1 + I/I_S}, \qquad (1.34)$$

where I_S is the saturation intensity.

Finally, we discuss the frequency dependence of the absorption rate, which is connected to the Einstein B factors above.

If all frequency responses (natural, Doppler and laser frequency profile) are approximated to Gaussian distributions the n-photon absorption rate can be obtained quite easily by the use of moment-generating functions as

$$R_n = \frac{\sigma_0^{(n)} \cdot G_n(0)}{(n\Delta\nu_L^2 + \Delta\nu_D^2 + \delta^2)^{1/2}} \cdot \frac{I^n}{(h\nu)^n} \cdot \mathrm{Exp}\left[-\left[\frac{\ln 16 (n\Omega_L - \nu_D)^2}{n\Delta\nu_L^2 + \Delta\nu_D^2 + \delta^2} \right] \right] \qquad (1.35)$$

In the expression some new parameters have appeared.

The index n corresponds to the number of photons involved in the excitation process.

$\sigma_0^{(n)}$ is the total absorption cross section.

The function $G_n(0)$ is the n'th order correlation function for the intensity fluctuations in the laser field.

The laser linewidth is given by $\Delta\nu_L$.

$\Delta\nu_D$ is the Doppler linewidth, $\Delta\nu_D = 2\nu_L \cdot \frac{\Delta v}{c} \cdot \sin\varphi$.

ν_D corresponds to the Doppler shift, $\nu_D = 2\nu_L \cdot \frac{v}{c} \sin\varphi$.

δ is the natural linewidth.

$I/h\nu$ is the laser photon flux.

Ω_L is the laser frequency offset from the line center.

This approximate description may well serve as a start to describe how the different broadening mechanisms influence the dynamics of atomic excitation under the influence of radiation.

2. Experimental considerations

2.1 Experimental techniques

The techniques discussed below can be described as being either time-resolved or wavelength-resolved, or simply spectroscopic. Some techniques that were developed before the laser era, e.g. th optical double resonance technique [2.1], are still employed. Together with the tremendous development of laser devices, an equal development of spectroscopic techniques took place and rendered some of the involved persons the Nobel prize.

Numerous laser techniques have been developed, e.g. saturation spectroscopy [2.2], intermodulated flourescence spectroscopy [2.3], polarization spectroscopy [2.4], intermodulated optogalvanic spectroscopy [2.5], frequency modulated spectroscopy [2.6], polarization intermodulated excitation spectroscopy [2.7] and high contrast spectroscopy [2.8].

Collimated atomic beam spectroscopy will be discussed in section 2.2.1 in conjunction with the description of the production of free atoms. The other spectroscopic techniques used in this thesis are quantum-beat spectroscopy (which will be treated under time resolved techniques) and saturation spectroscopy.

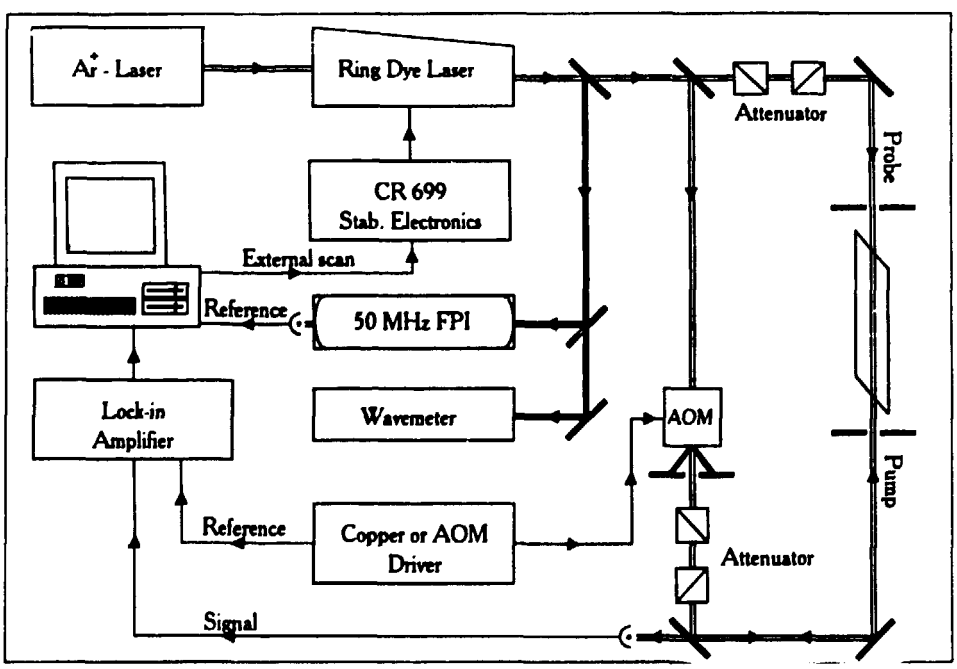

Figure 2. Experimental arrangement for saturation spectroscopy.

In saturation spectroscopy atoms are irradiated by a "monochromatic" laser beam, which leads to a change in population. Only a small group of atoms out of an inhomogeneously broadened Doppler profile can be in resonance with the light. This is depicted in figure 3a where the small resonant group of atoms have made a so called Bennet hole [2.9] in the velocity distrubution. This induced difference is probed with a counter propagating weak laser beam, e.g. by measuring the absorption of this "probe" beam when the laser wavelength is scanned. By monitoring the transmitted power of the probe beam, the results shown in figure 3b are obtained. The dip in the absorption profile is called a Lamb dip [2.10]. The line profile can be calculated using rate-equations. This is done e.g. in ref. [2.11], where the effects due to saturation are discussed. By lowering the laser power, the width of the Lamb dip will approach the natural linewidth.
Noise from AC power supplies (50 Hz) and from amplitude fluctuations in the laser amplitude, due to instabilities in the dye jet, can be lowered by modulation of the pump beam in combination with lock-in detection. This also has the advantage that the Doppler broadened absorption profile will disappear and leave the Lamb dip on a "zero" background as in figure 3c.

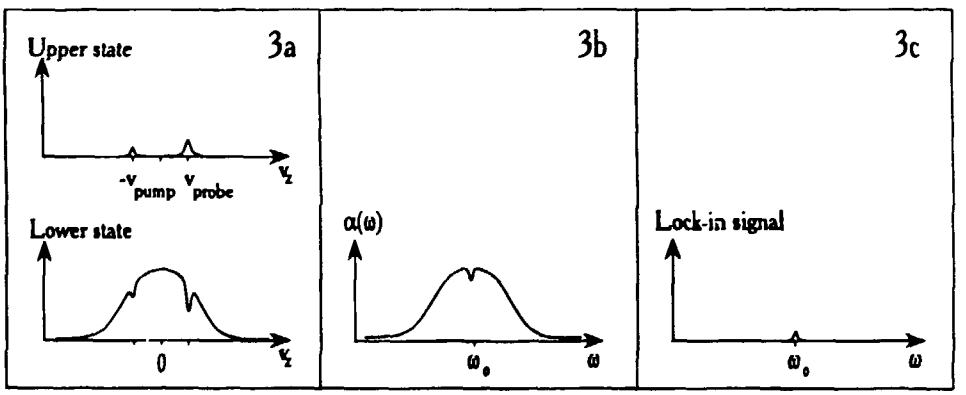

Figure 3. a) The velocity distribution of an upper and a lower atomic level resulting from the interaction with a pump and a probe beam. b) the resulting absorption of the probe beam. c) the absorption signal after lock in detection.

This is due to the fact that only variations in the probe beam in phase with the modulation of the pump beam yield a signal after lock-in detection. Sometimes a Doppler broadened background appears when "marked atoms" change their velocity in collisions so that the absorption

frequency gets Doppler shifted into resonance with the probe laser. This background can be lowered by increasing the modulation frequency. Another advantage with a high modulation frequency is apparent after examination of the noise spectra of a dye laser [2.12]. It should be possible to obtain a shot noise limited signal at modulation frequencies above 2 MHz.

One major drawback of saturation spectroscopy is the occurrence of cross-over signals which may complicate the analysis of the spectra. These occur when the two beams interact with the same velocity group on two different transitions as indicated in figure 4.

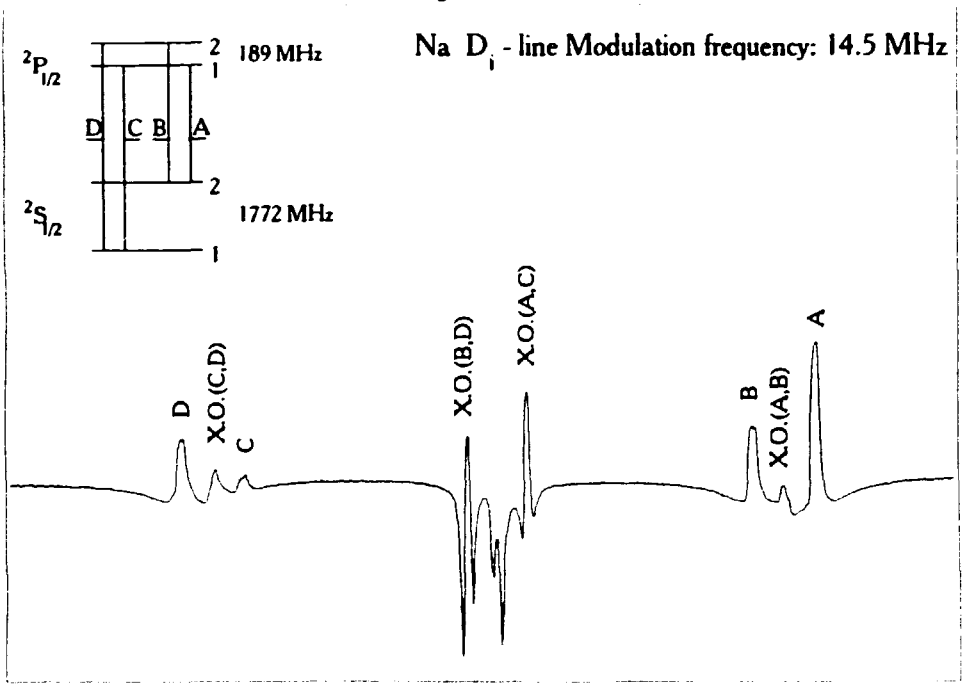

Figure 4. A spectrum recorded with the saturation spectroscopy technique. The pump beam was modulated at 14.5 MHz and a frequency mixer was used as a "lock in amplifier". The high modulation frequency resulted in distorted or reduced cross-over signals which simplified the interpretation.

Due to the large interest in lifetime data (or oscillator strengths) by theoretical atomic physicists, astrophysicists, laser designers and plasma physicists, quite a few time-resolved techniques have been developed [2.13].

So far the two most reliable laser techniques are the delayed-coincidence technique [2.14] and the fast beam laser technique [2.15]. These are not as commonly used as the more versatile pulse excitation (transient

recording) technique, where a laser pulse of 0.1 - 10 ns duration excites the atoms and the decay is captured by a fast photomultiplier connected to a transient recorder. For short lifetimes (on the order of the pulse length) the accuracy can sometimes be enhanced by recording the apparatus function for "deconvolution". Earlier the transient recorders were comparable to boxcar integrators, but today it is possible to get transient recorders with sampling rates of ~1 GHz at a reasonable cost. For fast processes a streak camera in combination with a picosecond tunable laser system may soon compete with existing techniques. When short laser pulses cannot be obtained, a technique which may be promising (using fast sampling techniques and powerful computers for the analysis of data) but has not yet proved to be competitive, is the so called phase-shift method [2.16]. Very good time resolution without the need for fast detection electronics can be obtained with the pump and probe technique, but unfortunately it works only for strongly absorbing media.

In this work the two techniques employed are the delayed-coincidence technique and the pulse excitation technique which will now be discussed.

The delayed-coincidence technique with single-photon counting utilizes a light pulse with a trailing edge short compared to the lifetime to be measured. A typical experimental arrangement is shown in figure 5.

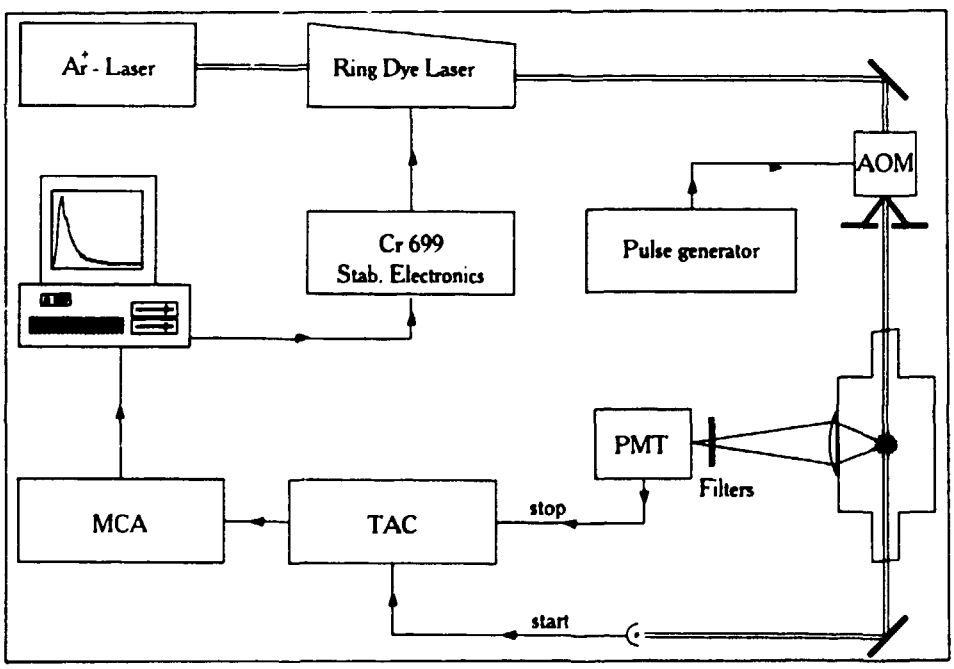

Figure 5. Arrangement for delayed-coincidence measurements.

The technique is based on measuring the time between excitation and de-excitation. The heart of the setup is the Time-to-Amplitude Converter (TAC), a fast clock measuring the time between the start and the stop photon. A small part of the laser light hits a fast photodiode to give a timing signal for the TAC to start (a start photon). The arrival of the stop photon is determined by the time it takes for an atom to be deexcited, according to the Poissonian statistics governing a radiative decay. The stop photons are normally collected at right angle to the laser beam and filtered through an interference filter before hitting the photomultiplier generating the stop signal for the TAC. The TAC becomes "dead" after the stop photon has arrived and sends out a voltage, proportional to the time between start and stop, to a multichannel analyser or a computer with a fast D/A card and appropriate software where a decay curve finally is obtained.

It is extremely important to avoid a count rate too high for the stop photons compared to the start photons, in order to avoid pile-up effects. This will destroy the statistics by measuring too few "long-lived atoms". The normal recommendation is to keep the count rate below 1 detected stop photon for every 30 start photons.

The main problem in measurements of fast decay rates is the jitter in the timing signals to the TAC. This problem is best solved by the introduction of fast constant-fraction discriminators for the start and stop pulses.

For further information on the subject we refer to the excellent book by O'Connor and Phillips [2.17].

The main advantage of the pulse excitation technique is the fast data aquisition times. In principle it is possible to measure a lifetime in one laser shot, i.e. a couple of lifetimes are needed to get a good enough curve. In contrast to the delayed-coincidence technique, there are some things which may affect the results. Nonlinearities in the detector (photomultiplier) must always be checked. Saturation of the atomic transition must be avoided if deconvolution with the apparatus function is done. These two things can quite easily be checked by comparing the signal strength with and without grey filters with known transmission. The data cannot be used for statistical tests of the quality of the decay curve unless the the number of photons for each point is known.

Further error sources for these kinds of measurements will be discussed in section 2.4.2.

2.2 Production of free atoms by evaporation techniques

2.2.1 Cell and collimated atomic beam measurements

The two most important applications for collimated atomic beam and cell measurements are high-resolution spectroscopy and time-resolved spectroscopy.

If a cell or a beam experiment is to be preferred depends on a number of different aspects, e.g. the temperature required to obtain a sufficient vapour pressure may be too high for a glass cell. There is also the possibility to achieve a metastable population (or ions) by applying a discharge and letting the released electrons collide with the atoms.

High resolution can only be obtained if the Doppler broadening of the atomic resonances can be overcome in some way. One of the easiest spectroscopic methods available to reduce the Doppler broadening is the collimated atomic beam technique. Another method used in cell measurements is saturation spectroscopy, where the Doppler broadening can be eliminated (i.e. the first-order Doppler effect).

In a collimated atomic beam experiment an oven, constructed of e.g. steel,aluminum oxide or boron nitride, contains a sample of the material to be studied. A tungsten wire is wound around the oven for resistive heating. The heated sample then evaporates and atoms effuse out of a small hole, into a vacuum chamber, forming the atomic beam. For the velocity distribution given in the following to be valid, the requirements on the size of the small hole is that it should be much smaller than the mean free path in the oven. There are, indeed, some important advantages in having a "long" hole described in [2.18]. The beam is collimated with a slit, of a width b, at a distance r from the oven (figure 6).

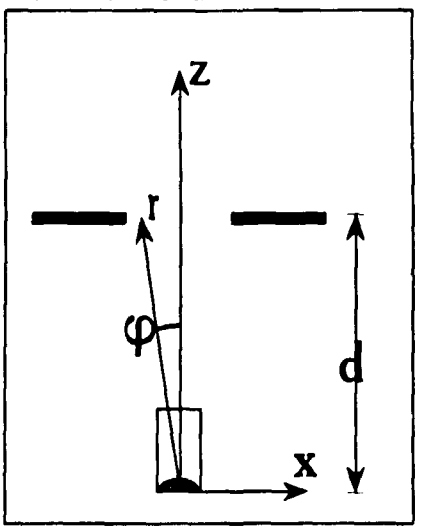

Figure 6. A schematic of the collimated atomic beam with the variables used in the text.

The velocity distribution in the beam is a Maxwellian transmission distribution according to [2.19] and [2.20]:

$$W_{beam}(v) \propto v \cdot \cos\varphi \cdot W_{cell}(v) \qquad (2.1)$$

v is the absolute mean velocity $|v|$, φ = arctan(x/r) is the angle from the oven normal and $W_{cell}(v)$ is the Maxwellian velocity distribution valid for an atomic gas contained in a cell at some equilibrium temperature T

$$W_{cell}(v) = 4\pi\,(M/2\pi kT)^{3/2}\, v^2\, e^{-(v/v_P)^2} \qquad (2.2)$$

The most probable-, mean- and root-mean square velocity v_{mp}, v_m and v_{rms} given in units of v_P ($v_P = \sqrt{2kT/M}$) are [2.18]:

	Cell	Atomic beam
v_{mp}	1	$\sqrt{3/2}$
v_m	$\sqrt{4/\pi}$	$\sqrt{9\pi/16}$
v_{rms}	$\sqrt{3/2}$	$\sqrt{2}$

Thus, the velocities are somewhat higher in the case of an atomic beam. The density in the atomic beam for the velocity component v, at a distance r from the oven is [2.20]

$$n(v,r) = \frac{4\cos\varphi}{\sqrt{\pi}\, r^2} \cdot (v/v_P)^3 \cdot e^{-(v/v_P)^2} \qquad (2.3)$$

with $\cos\varphi = z/r$.

The resulting line profile can be obtained by integrating the product of the atomic density and the Lorentzian absorption cross section over the velocity as well as over the slit width (from x_1 to x_2)

$$I(\omega) \propto \int_{v=0}^{\infty} \int_{x=x_1}^{x_2} \frac{n(v,r)\, dx\, dv}{(\omega-\omega_0-kv\sin\varphi)^2 + (\gamma_s/2)^2} \qquad (2.4)$$

with $\sin\varphi = x/r$.

From algebraic arguments we see that the Doppler width is (approximately) reduced by the collimation ratio

$$\Delta\omega_D^{coll} = \Delta\omega_D \cdot \sin\varphi \approx \Delta\omega_D \cdot b/2d \qquad (2.5)$$

where φ is the angle from the oven normal to the slit edge (assuming the slit to be centered over the oven). This will give a total line width of

$$\Delta\omega_{tot} = \sqrt{\gamma^2 + (\Delta\omega_D \cdot \sin\varphi)^2} \qquad (2.6)$$

However, to obtain the exact value of $\Delta\omega_{tot}$, the integral must be solved numerically. Figure 7 shows a recording of the hyperfine structure for the singlet-triplet mixed 5s19d ($^1D_2 + ^3D_3$) states in strontium obtained using an atomic beam with a collimation ratio of 1:20 (from paper 1). Similar

techniques not discussed here, e.g. the heat pipe technique [2.21] can be found in reference [2.22].

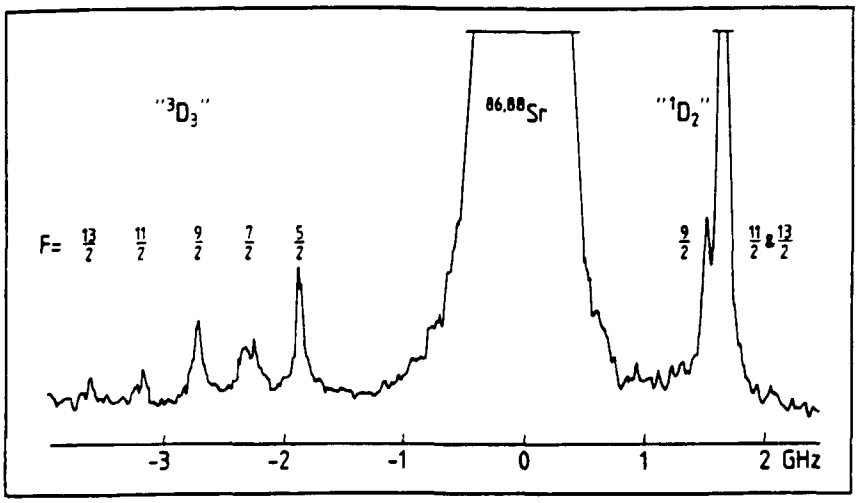

Figure 7. Hyperfine structure in a singlet-triplet mixed state obtained using the collimated atomic beam technique. The collimation ratio of 1:20 resulted in a linewidth of ~ 80 MHz.

2.2.2 Production of atoms by sputtering in hollow cathodes

Sputtering in a hollow cathode can be advantageous for studying refractory elements and rare gas atoms, especially since a high population can be obtained in high-lying metastable states. Furthermore, some transition elements with extremely high evaporation temperatures (a 0.01 mbar vapour pressure at temperatures between 2000 and 3000 K), e.g., Sc, Y, Ti, Zr, Hf, Mo, W, Tc, Re, Os, Rh, Ir and Pt which are not suited for atomic beam measurements, can be sputtered in a hollow cathode. However, the yields are normally quite low.

The mechanisms of the sputtering process have been extensively examined [2.23] and are thus quite well understood. The sputtering yield [2.24] is best for elements with more than half-filled d shells. The yield also depends on the masses of the involved species in such a way that if the cathode material and the carrier gas atoms have the same masses, the sputtering yield will be optimized. In ascending order the "best" sputtering (with Ar^+ bombardment) is obtained for Ag, Au, Pd, Cu, Ni, Pt, Cr, Co, Fe, Ge, Ru, Ir, Al,... For Mo, Ta and W, which were mentioned as not suitable for resistive heating, the sputtering yield is about 4 times lower than for Ag, Au, Pd and Cu. Two different types of hollow cathodes

have been employed in paper 3 and 4. The different advantages in specific experimental situations have also been discussed in paper 7 and a more extensive discussion of the two types may be appropriate here.

The first type of hollow cathode to be discussed (Constructed by S. Kröll [2.25]) was designed according to the descriptions by Lawler *et al.* [2.26]. The cathode is formed as a cylinder, where a cylindrical target foil could be placed near the center, inside a cell with the anode a couple of centimeters away. The cell is equipped with quartz Brewster windows and connected to a gas handling system. This cathode produces a dense plasma which is well suited for saturation spectroscopy measurements. An almost field free region is obtained with the cylindrical cathode arranged so that the negative glow discharge region, where the electrostatic potential is almost constant, becomes the region which is probed by the counter propagating laser beams going through the cell.

Normally this cathode was operated with Argon as a buffer gas at pressures around 0.5 mbar and a current of 200 mA. Running the hollow cathode under these conditions, using a cylindrical target foil made from copper, electron and atom densities of 10^{12}- 10^{13} cm^{-3} could be obtained.

The second hollow cathode was a large bore low pressure diffusive type, constructed by following design rules like the similarity rule [2.26]. The construction is shown in figure 8.

The Pyrex glass tube has an inner cylinder which serves as a guide for the ions in the discharge which sputters the target foil (and the cylinder foil) on the cathode bottom plate. This construction differ somewhat from what is normally seen in the literature and the main advantage is an improvement in the atomic and ionic density of the sputtered material close to the bottom of the cathode where the hole is. If the discharge is to be run for a longer period of time, there will be problems with cathode material sticking to the inner glass tube which finally destroy the discharge. This is a problem for both types of constructions, however, since less material needs to be sputtered to achieve the same density outside the hollow cathode, the latter type of construction is somewhat better in that respect. It will also be possible to have a larger pressure gradient and still sustain a DC discharge. This may be interesting when running the discharge in a pulsed mode in order to achieve higher peak currents and thus higher ion to atom yields as well as higher densities of sputtered material. It is important to have sufficient cooling on the end part of the cathode to minimize problems with material sticking to the

glass and the cathode bottom plate.

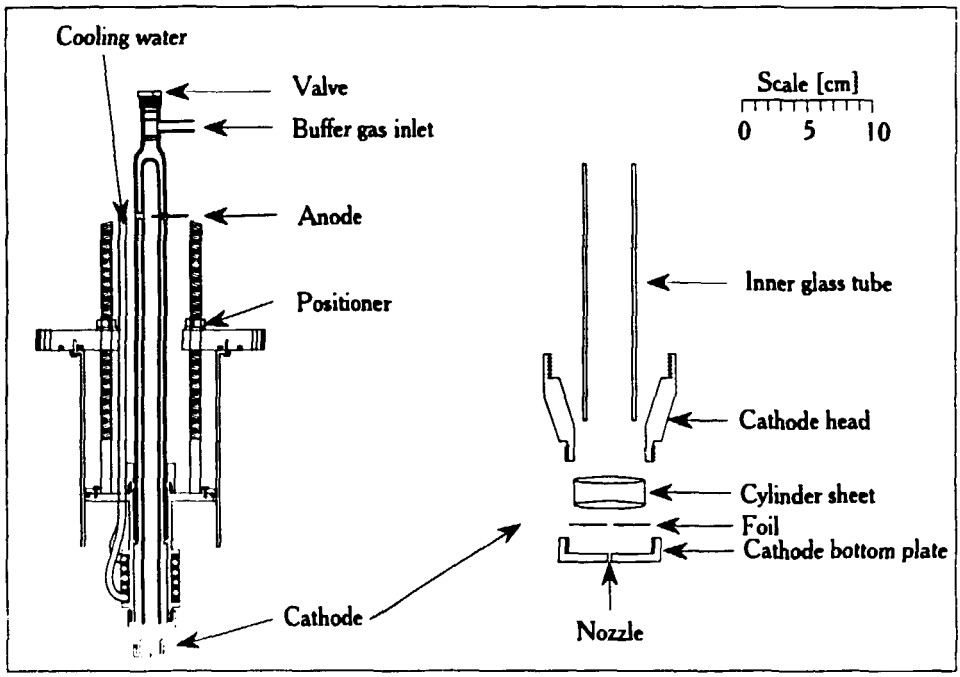

Figure 8. The outline dimensions of the effusive hollow cathode.

The hollow cathode was normally operated with Argon as a buffer gas at pressures of 0.5 mbar. A small hole in the cathode bottom plate served as a nozzle for forming the atomic beam which effuses into a vacuum (10^{-4} mbar) scattering chamber. Collimation of the atoms, before intersecting the atomic beam with the laser beam, is now possible. The DC current was normally kept at 150 mA (with a potential drop over the hollow cathode around 500 V). The bottom cap is exchangeable and made of Cu, Fe or brass depending on the material in the thin target foil placed in the bottom cap. A cylindrical foil in contact with the target foil to make a cup was sometimes used to increase the sputtering yield.

It was noticed, (in the experiments on Gd II) that higher efficiencies could be obtained with Gd target foils by using tantalum in the cylinder foil. Since both Ta and Gd have less than half filled 5d-shells the sputtering by Ar should be equally efficient. The atomic mass difference is somewhat smaller for ^{157}Gd than for ^{181}Ta as compared to ^{40}Ar. The main difference was the possibility to obtain a smooth clean surface of the different target materials. The tantalum foils could be polished to a much

higher degree, which ensured better working conditions. This must be the explanation to the increased Gd II yield when using Ta in the cylinder foil. The foils as well as the glass tubes were always thoroughly cleaned with ether and the system was run for about one hour in DC mode before the measurements were performed. When the colour of the discharge was violet, the best results were obtained, a whiter shade indicates that oxygen is present which quickly deteriorates the target foil.

Measurements on tantalum ions in metastable states, as high as 11 000 cm^{-1} above the ground state, all reported in paper 3 using the above mentioned DC current and pressure but with the addition of electrical discharge pulses produced from a thyratron switched capacitor. The discharges were transformed to peak powers around 20 kW with 10 μs duration.

The discharge in the first type of hollow cathode produces a much denser plasma than the second one. This makes it better suited for Doppler-free saturation spectroscopy. However, problems with pressure broadening and Stark shifts may occur even if the measurements are performed in the negative glow discharge region, where the electrostatic potential is almost constant.

Such problems can be avoided with the diffusive type of discharge in which a beam of free atoms emerges from the plasma. However, the effects of the field from ions and electrons in the atomic beam have not been examined and could give rise to problems when an extremely field free environment is required. A situation where this type of atomic beam will give rise to similar problems is when detection of ions or electrons are chosen in favour of photons. This was a problem we tried to overcome in some preliminary experiments by using deflection plates and Faraday cages to screen out electrons and ions from the detection volume where a channeltron for the detection of photo electrons was placed. The electronic and ionic backgrounds could, however, not be lowered sufficiently for the channeltron to work properly.

The intensity of the laser light in the UV region is normally too low for saturation spectroscopy, why the diffusive type of hollow cathode is the more versatile one here.

A lot of effort is being put into measuring atomic and ionic properties of light elements (especially oscillator strengths) where the resonance lines are in the VUV-wavelength region. However, since the lifetimes become shorter, the high pressure in the first type of hollow-cathode discharge is less critical for accurate lifetime determinations. An interesting way

to increase the sensitivity for the first type of discharge is to use auto ionizing levels to do resonance ionization combined with optogalvanic detection.

Using the second type of discharge in a pulsed mode has proved to be a very efficient way to increase ion yields and it might be successful to try this with the other type of hollow cathode discharge.

A similar technique to obtain atoms and ions in excited states is to use a radio-frequency discharge, e.g. in a cell. The RF transmitter is constructed with a coil surrounding the sample cell, which is a part of the resonance circuit. When this is balanced close to resonance, optogalvanic detection of the signals is possible. In combination with laser excitation of atoms or ions to auto-ionizing states, optogalvanic detection is one of the most sensitive techniques known.

2.2.3 Production of atoms by laser evaporation

As discussed, elements with extremely high evaporation temperatures are not suited for the production of free atoms using standard methods, such as evaporation from an oven. The list of elements given above is in no way complete, e.g. the theoretically interesting light elements boron, silicon and carbon should be included in the list. However, these elements are not suited for hollow-cathode measurements either, since B, Si and C are semiconductors and isolators with a too low conductivity.

The laser-produced plasma has been examined earlier by e.g. Bolan et al. [2.27] using mass spectroscopy. It is, however, a rather novel source for the production of free atoms, ions, molecules and clusters as applied to laser spectroscopy.

In our experiments, the plasma was normally produced by focusing a Nd:YAG laser with a power of 25 mJ and a duration of 7 ns with a 25 cm lens onto a rotating target, placed in a high-vacuum chamber (10^{-6} mbar). The behaviour of the plasma itself is interesting to study and a lot of theoretical and experimental work has been carried out, mainly due to the possibility of achieving controlled fusion in laser produced plasmas [2.28]. We have measured radiative lifetimes, hyperfine structure, absorption cross sections, ionization cross sections, stimulated emission and the electron density using laser-produced plasmas (papers 5, 6, 9 and 11).

The experiments have clearly demonstrated that although the environment in the plasma plume is rather hostile, it is possible to perform accurate determinations of spectroscopic properties. The species examined in our laboratory until now are B, C, Al, Si, Fe, Ta and W. Interesting properties of a plasma, e.g. velocities and densities of electrons, atoms and ions, have been examined somewhat by studying the emission and the integrated refractive index of the plasma. When examining the plasma we made recordings of fluorescence spectra both time integrated and, for specific transitions, time resolved. Figure 9 shows the spectra of B with the different ionization stages indicated. The upper part of the spectra was obtained using a standar spectrometer and photomultiplier. The lower part of the spectra (in the VUV region) was recorded with a home built vacuum spectrometer equipped with an electron multiplier tube giving a much poorer resolution.

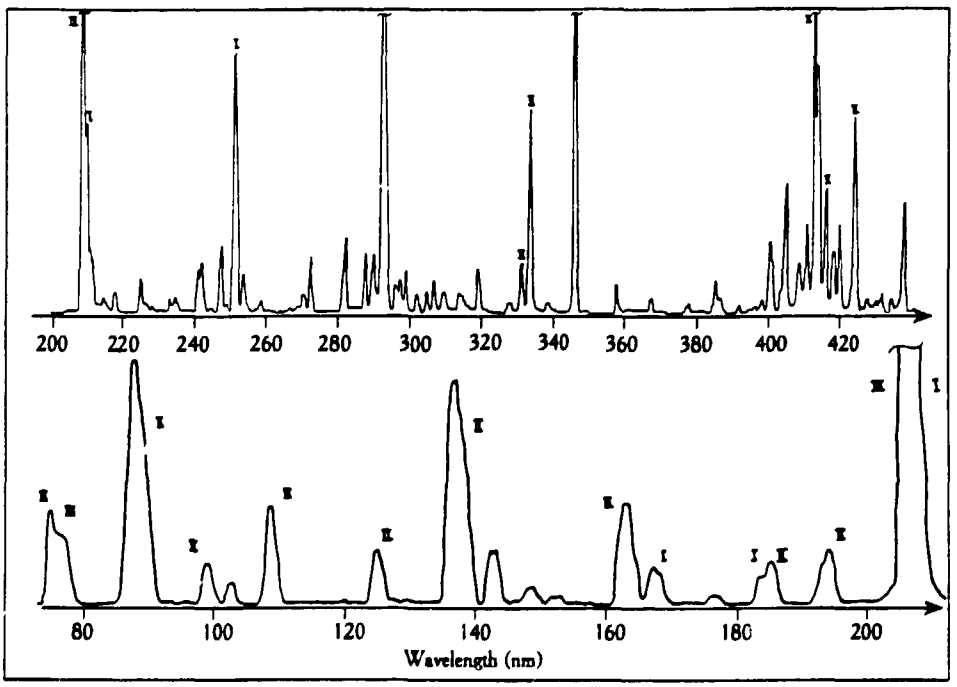

Figure 9. Two spectra obtained from a laser-produced plasma. The indices belong to different ionization stages of boron

Figure 10 shows the time-resolved fluorescence of three specific transitions in B I, II and III, as a function of distance from the target.

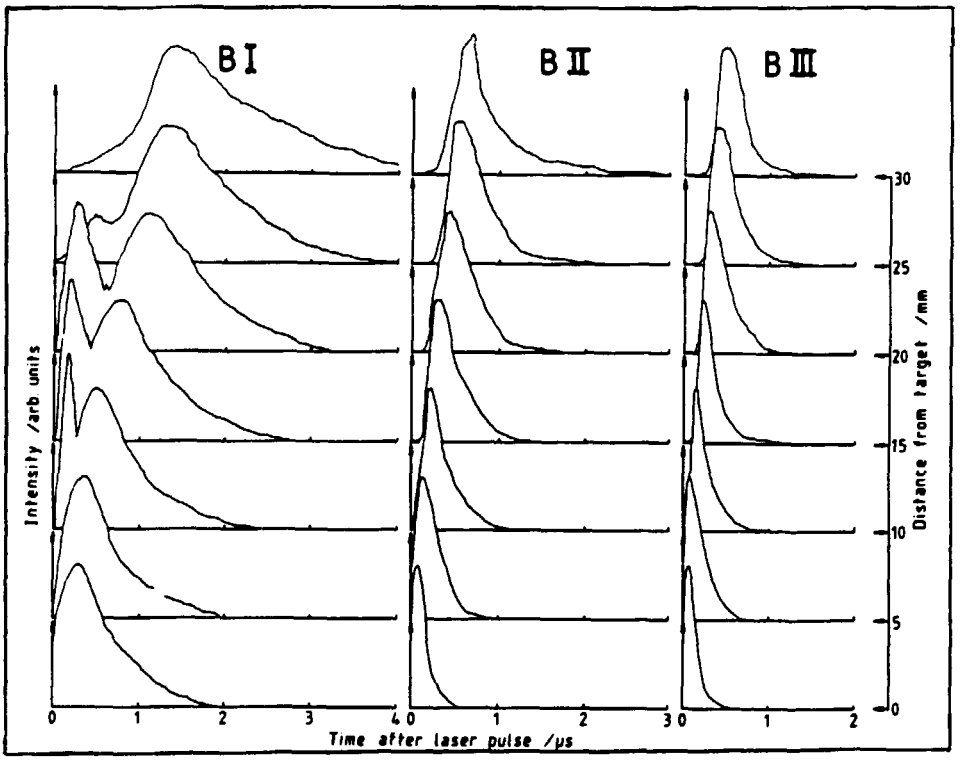

Figure 10. Time resolved spectra of boron in a laser-produced plasma.

Laser-produced plasmas are interesting as media for XUV or VUV lasers [2.29]. By examining spectra like the ones in figure 9 and 10, one might find new candidates for laser transitions. E.g. the early peak seen in some of the time-resolved recordings for B I is due to three-body recombination. This process can give rise to population inversions. Investigations of the amplification and the absorption in an aluminum plasma are currently being performed in our laboratory.

When the measurements on carbon were performed we happened to re-discover the influence of ASE or Stimulated Emission on lifetime measurements. This led to the idea that the SE process itself might be utilized in concentration measurements. A rate equation analysis was performed (to be discussed in section 2.4.3) in order to check to what extent the ASE influenced the Laser Induced Fluorescence (LIF) signal, which is the normal tool for concentration measurements [2.30].

The rate equations were also used in a calculation of excitation line profiles in order to check if the Doppler profiles agreed with the velocity parameters obtained from the kind of spatially and time-resolved fluorescence measurements shown in the figure above. The best fit to the

experiment for the specific conditions was obtained with a mean velocity $v = 14 \cdot 10^3$ m/s and a velocity spread of $\Delta v = 7 \cdot 10^3$ m/s.

2.3 Excitation of atoms

The first laser was constructed by T.H. Maiman in 1960. It was a flash-lamp pumped ruby laser with a pulse duration of 1 ms [2.31]. After the discovery of laser action in organic dyes in 1966 [2.32], the development of lasers as spectroscopic tools set full speed. It would be impossible to include the history of laser technology or to give a description of the numerous devices utilized today. Therefore, only some of the lasers used in the experiments of this thesis will be discussed.

Dye lasers with wavelength-selective elements inside the laser resonator made it possible to obtain tunable narrow-band radiation over a large spectral range [2.33]. The commercial ring dye laser (Coherent Radiation CR-699-21) used in papers 1 and 2 is quite easily tunable in the region from 400 to 800 nm with an output power of 50-800 mW, depending on the dye efficiency and the quality of the optics. The linewidth should correspond to 1 MHz according to specifications and the sharpest spectral feature tested on this particular laser, to my knowledge, was a 2 MHz broad iodine saturation spectroscopy signal. This corresponds to a wavelength resolution of $\Delta\lambda/\lambda \approx 2 \cdot 10^{-9}$.

In paper 7 an intracavity frequency doubling crystal was installed in the ring laser. With this technique the wavelength region could in principle be extended down to 200 nm but the output power will be less than 2 mW. The linewidth should then only be increased by a factor of $\sqrt{2}$.

The main drawback of the dye laser is the amplitude fluctuations due to instabilities in the dye jet, which give rise to noise in the measurements. This has been thoroughly examined by Hänsch, Hall and others in their quest towards the ultimate resolution. So far laser linewidths of around 1 mHz have been achieved. The setup for a collimated atomic beam experiment utilizing the ring-dye laser is schematically outlined in figure 11.

Unfortunately, the output power of the dye lasers are often not high enough for lifetime measurements in the UV-region, where the largest demands for accurate lifetime data are. This is the main reason why a pulsed laser system was used in most of the papers (paper 1-6, 9 and 10).

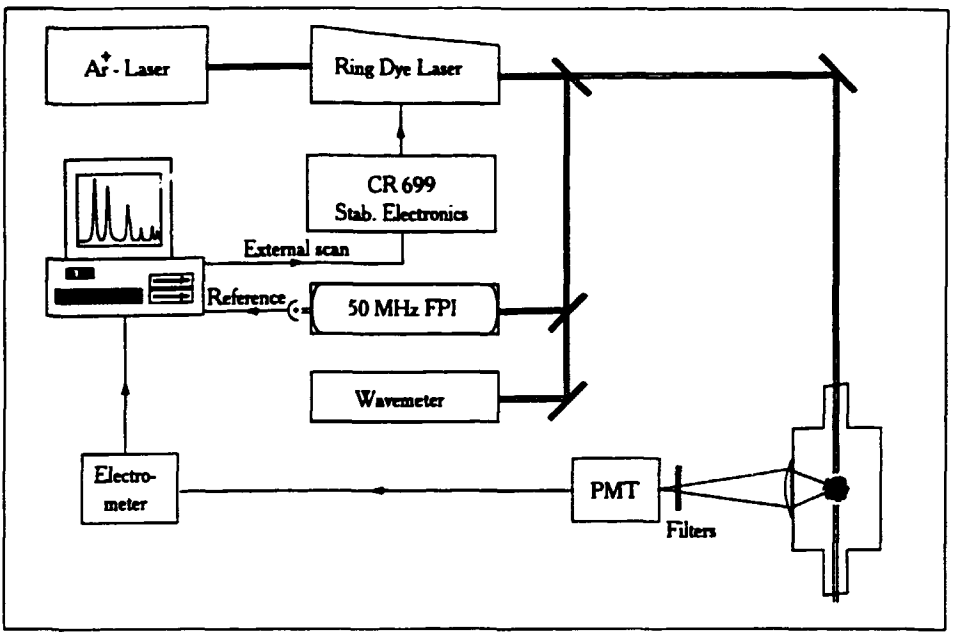

Figure 11. Experimental arrangement for collimated atomic beam spectroscopy. The oven and collimation slits, depicted in figure 6, are positioned inside the vacuum system to create a beam of atoms at right angles to the laser beam as well as to the direction of detection.

The pulsed system is also a commercial device from Quanta Ray (DCR-2 Nd:Yag laser and a PDL-1 dye laser). It is a flashlamp-pumped Nd:YAG laser with a fundamental frequency of 1.06 μm, which can be frequency doubled to 532 nm (and, if needed, optics for generation of the third and fourth harmonics at 355 and 266 nm are available). This laser is used to pump the PDL-1 dye laser to produce tunable radiation in the region 300-800 nm with a pulse duration of ~7 ns and a pulse energy of ~50 mJ, which corresponds to a peak power of 7 MW. The bandwidth is ~0.3 cm^{-1} (≈ 7 GHz). This linewidth is matching the Doppler broadening of the atomic transitions (1-10 GHz). Comparing the spectral brightness (spectral energy density within a unit frequency interval) of the ring dye laser with the pulsed dye laser, the latter is a factor of ~3000 higher ($1.5 \cdot 10^{-3}$ W/Hz as compared to $5 \cdot 10^{-7}$ W/Hz).

Extension of the wavelength region with the use of nonlinear optics is possible using frequency doubling, mixing and Raman shifting. For a discussion of such processes we refer to the book of Shen [2.34].

In paper 13 on light-in-flight holography we used a laser system capable of producing pulses with a length of 10 ps at a maximum repetition rate of 37 MHz and an average power of 50-200 mW in the wavelength region 560-630 nm. This commercial "picosecond" system (from Coherent Radiation) consists of a mode-locked argon-ion laser (CR 12) pumping a linear dye laser (CR 599) with a delay line to match the cavity length and a cavity dumper controlling the repetition rate (i.e. the number of cavity round trips before ejection from the dye laser).

2.4 Analysis of data and sources of error

2.4.1 Hyperfine structure

The hyperfine structure can be evaluated using a simplified Hamiltonian which, in the absence of external fields, may be written as

$$H_{hfs} = a\mathbf{I}\cdot\mathbf{J} + \frac{b}{2I(2I-1)J(2J-1)}\left[3(\mathbf{I}\cdot\mathbf{J})^2 + \frac{3}{2}(\mathbf{I}\cdot\mathbf{J}) - \mathbf{I}^2\cdot\mathbf{J}^2\right] \qquad (2.7)$$

This operator results in energy shifts according to

$$E_{hfs} = \frac{a}{2}C + \frac{b}{2I(2I-1)J(2J-1)}\left[\frac{3}{4}C(C+1) - I(I+1)J(J+1)\right] \qquad (2.8)$$

with $C = F(F+1) - J(J+1) - I(I+1)$ (2.9)

The hyperfine spectrum may not always be as simple as to contain only this information. The spectra below showing a recording of the $3d^94s^2\ ^2D_{3/2}$ to $3d^{10}5p\ ^2P_{1/2,3/2}$ transitions in both isotopes of copper will not reveal all information on the upper state hfs structure and will only yield a crude guess of the a factors.

As the lower state has larger splittings both a and b factors of both isotopes are readily obtained. Furthermore, the fine-structure splitting between the $^2P_{1/2}$ and $^2P_{3/2}$ states as well as the isotope shifts can be determined with high accuracy. The split spectrum in figure 12 indicate the disentanglement of the spectroscopic data.

In order to optimize the signal-to-noise ratio on the weaker $^2P_{1/2}$ transitions, the spectrum was recorded by changing the detection wavelength during the frequency sweep right after the first three peaks belonging to the $^2P_{3/2}$ state.

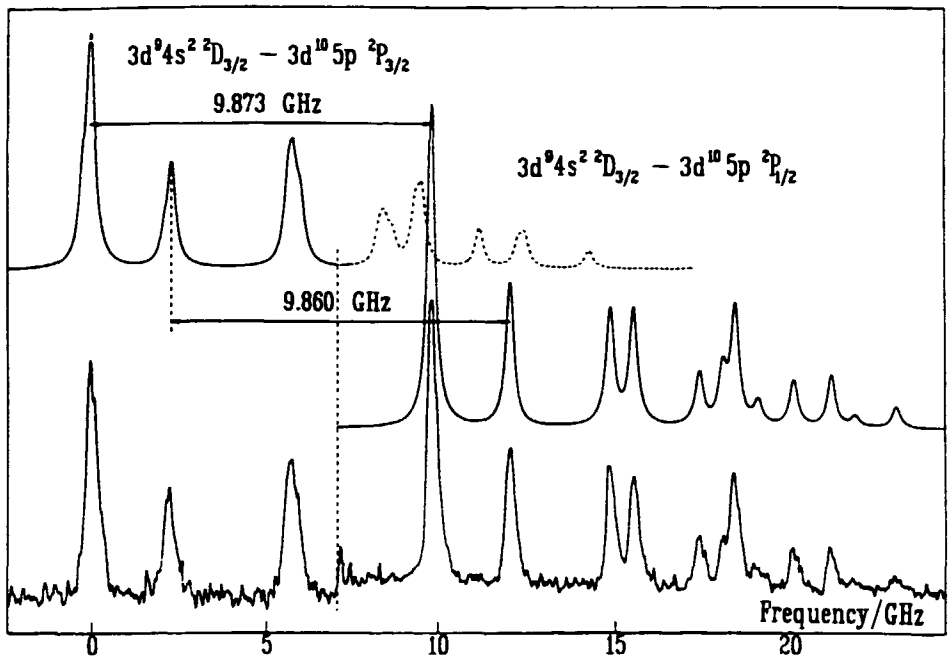

Figure 12. A hyperfine structure recording in copper obtained using collimated atomic beam spectroscopy.

For the high-resolution measurements on copper (paper 7) a program package was developed. The program consist of an acquisition part and an evaluation part and is presented as a Department Report (paper 8). The acquisition is performed by using the analog output of a A/D-D/A card for laser frequency control and two input channels for simultaneous recording of frequency calibrating interference fringes and the signal. The evaluation is performed by linearising the frequency scan by fitting a polynomial with a degree of 5-9 to the peak positions of the recorded 50 MHz interference fringes. The scan of the dye laser is normally not linear, which is mainly due to temperature drifts in the laser reference cavity. After selection of a number of peaks, the program fits either Gaussian or Lorentzian shaped peaks to the spectrum, using Newton's method for least-squares fitting.

Quantum beats in decay curves open up another possibility to obtain information about the hyperfine structure with time-resolved measurements. The quantum beats in the total fluorescence from a superposition of states may appear if a short laser pulse excites a distribution of closely spaced states, all within the bandwidth of the laser. The main difference between quantum-beat spectroscopy and evaluation of hyperfine spectra is that the QB signal contains information only on the splittings in the upper state.

The beats occur at the difference frequencies, why it is more difficult to distinguish between different isotopes. Another important aspect is the fact that the sign of the a and b factors cannot be established in a QB measurement. This is true at low atomic densities when interference between decay amplitudes of two or more atoms can be neglected. Collective quantum beats have not been observed so far. Allthough, similar types of experiments have been performed when a macroscopic optical dipole has been prepared in the medium. The beats or echoes in such cases may, however, be interpreted as interference effects in excited and ground state level splittings [2.35].

A program referred to as LTQB in [2.18] was used for the evaluation of quantum beats and decay rates. The principle of the evaluation is the following. The lifetime is evaluated by fitting an exponential plus a background to the recorded signal using a nonlinear least-squares technique. The recorded curve is divided by the fitted exponential and centered around zero. After apodization with a suitable window, to suppress side lobes, Fourier transformation is performed. The peak positions in the frequency domain corresponding to different splittings are then localized.

2.4.2 Lifetimes

In the analysis of decay rates it is appropriate to consider some important systematic errors which may occur. As previously discussed, quenching collisions will shorten the lifetime. This effect is normally of the order of 10^6 $s^{-1} \cdot mbar^{-1}$, i.e. the contribution to the decay rate at pressures of 10-100 mbar is normally larger than the natural decay rate. Since quenching is proportional to the pressure, it is possible to extrapolate the measured decay rate towards zero pressure to obtain the unperturbed lifetime (Stern-Vollmer plot). There is, however, one other possible source of error connected to measurements at high atomic densities. If the studied state is coupled to the ground state with a high transition probability, (short-lived state) the emitted photons will have a large probability of being reabsorbed several times before reaching the detection system. This is referred to as multiple scattering or photon trapping. This effect was studied in paper 10, where the trapping was utilized to obtain both the branching ratio to the ground state and the

decay rate. This is shown in figure 13, where the straight line intersects the y-axis at a point referred to as the totally trapped decay rate: the decay rate A minus the decay rate to the ground state A_g.

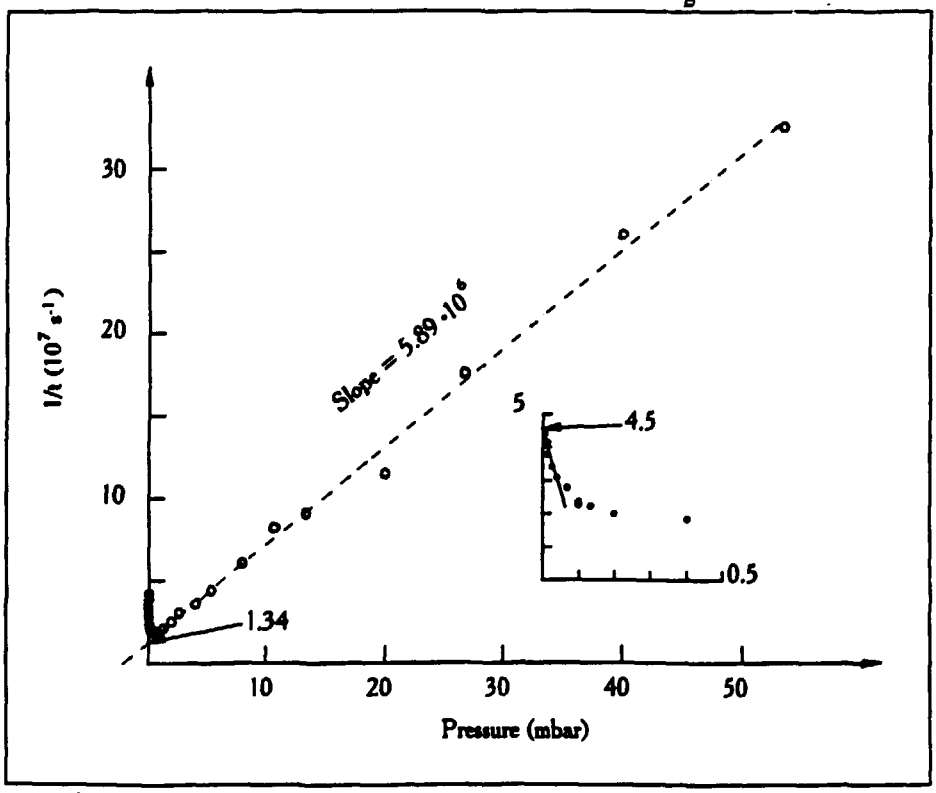

Figure 13. Stern-Vollmer plot of the decay rate for the B state in CO

When the excited atoms have a large enough probability to leave the detection volume before being deexcited, this will cause a reduction in the measured lifetime (flight-out-of-view effect). The effect may occur when studying long lifetimes in atomic-beam experiments. In a laser-produced plasma the velocities are a factor of 10-100 larger which limits the range of lifetimes possible to study even more.

Finally, it should be mentioned that magnetic fields will give rise to Zeeman quantum beats which occur due to interference between the magnetic sublevels. There are three solutions to the problem. A field-free detection volume may be obtained by using Helmholtz coils to compensate for the external fields. One might also apply a magnetic field strong enough to make the beat frequency higher than the sampling frequency of the detection electronics. When using linear polarizers, the amplitude of the beats is described by the Legendre polynomial $P_2(\cos\theta)$ which is zero

for $\theta = 54.7^{o}$ ("magic angle"). Here θ is the angle between the excitation and the detection polarization vectors in a 90^{o} detection geometry.

Stark effect during the excitation is also a possible source of error if the evaluation is performed during the laser pulse, as is the case for deconvolution techniques. The only way around this problem is to start the evaluation of the decay curve after the laser pulse has ceased.

It is sometimes observed that pulsations in photomultipliers or channel plates give rise to a secondary peak, resembling the electrical reflections obtained with mismatched connectors. If the pulsation cannot be removed it is necessary to perform a convolution during the evaluation of the decay rate.

Unfortunately, we have been forced to used the deconvolution technique in combination with two-photon excitation in some cases. However, this need not be totally incorrect, at least not when the main contribution to the response function is due to the detectors and electronics.

A program developed by A. Persson [2.18] was utilized for the evaluation of decay rates by fitting to a laser pulse convolved with an exponential, background and stray light. Several programs exist for the interfacing of an IBM/(XT, AT or 386) machine with different devices, as e.g. a Biomation 8100 transient digitizer and a Tektronix 2431L digital oscilloscope. The program package for evaluation of data is used on the same computer.

In astrophysics and other applications the decay rate needs to be quantified, which can be done in several different ways. The technique used in paper 4 is based on the sum rule for the A factors in equation 1.21. By measuring the lifetime of the excited states and scanning the emission spectrum, the different line strengths can be compared and related to branching ratios. By normalizing the branching ratios with the decay rate we obtain the A factors. If these numbers are multiplied by the multiplicity g_j, we get gA values (paper 4). Problems with this technique are the relative calibration of the wavelength dependent transmission of the detection system and the risk of missing lines in the infrared or ultraviolet regions outside the detection limits.

Another possibility would be to make an absolute calibration of the detection equipment for an experimental situation where the number density of the atoms and the relevant laser parameters are known. Several techniques have been developed to perform calibrations necessary for absolute measurements, e.g. by using Raman scattering, but these will not be discussed here.

2.4.3 Stimulated emission and density measurements

In combination with the measurements on C discussed in paper 9 and CO in paper 10, the dynamics of the populations of the different levels were simulated using rate equations. The programs developed will be discussed below, starting with the calculations on carbon.

The measurements on carbon were performed in a laser-produced plasma. The calculations were difficult due to inhomogeneties along the laser beam, with large Doppler shifts and velocity spreads in the rapidly expanding plasma. Due to this the accuracy of the calculations was not good enough to be used for further developement of a macroscopic code to calculate the amount of stimulated emission obtained. The calculations on CO on the other hand were complicated due to the many levels involved in combination with uncontrollable rotational and vibrational relaxation processes. The main advantage of CO was the possibility to obtain a rather long homogeneously pumped region which in turn made an analysis of the stimulated emission possible.

The rate equations were used in a procedure where the atomic density was fitted to the fluorescence yield as a function of the laser power. The populations on the different levels involved are calculated using the following set of levels in the rate equations: $2p^2\ ^3P_2$, $2p3p\ ^3P_2$, $2p3s\ ^3P^o_2$, $2p3s\ ^3P^o_1$, $2p^2\ ^3P_{1,0}$ and C II.

The two-photon rate, W_{12} is determined by the linewidth of the laser, the width of the atomic transition and the Doppler broadening. This is taken into account using the following relation

$$W_{12} = \sigma_0^{(2)} \frac{G_2(0)}{\sqrt{2\cdot\Delta\nu_L^2 + \Delta\nu_D^2 + \delta^2}} \cdot \frac{I^2}{(h\nu)^2} \qquad (2.10)$$

The cross section is calculated according to [2.37]

$$\sigma_0^{(2)} = \frac{6.2\cdot 10^{-25}\ h\ \nu^2}{\Delta E_{il}^2} \cdot |\mu_{gi}|^2 \cdot |\mu_{ie}|^2 \cdot g(\omega) \cdot f \qquad (2.11)$$

$|\mu_{gi}|^2$ is the transition dipole moment going from $|g>$ to $|i>$ and $g(\omega)$ and f include the frequency dependence and the laser coherence properties. However, in a laser-produced plasma, the velocity distribution is not homogeneous over the interaction volume. Because of this the correction for the linewidth may have to be modified. We introduced a z-dependence of the two-photon cross section by using the projection of the atomic velocities on the z-axis, given by $\tan\theta = z/L$, where L is the distance

from the target to the interaction zone. Implementing this in the two-photon absorption rate, with the Doppler shift ν_D

$$\nu_D = 2\nu_L \cdot \frac{v}{c} \cdot \tan\varphi \tag{2.12}$$

and the Doppler width $\Delta\nu_D$ given by

$$\Delta\nu_D = 2\nu_L \cdot \frac{\Delta v}{c} \cdot \tan\varphi \tag{2.13}$$

we obtain

$$W(z) = \frac{\sigma_0^{(2)} \cdot G_2(0)}{\sqrt{2\Delta\nu_L^2 + \Delta\nu_D^2 + \delta^2}} \cdot \frac{I^2}{(h\nu)^2} \exp\left[-\left[\frac{\ln 16 \cdot (2\Omega_L - \nu_D)^2}{2\Delta\nu_L^2 + \Delta\nu_D^2 + \delta^2}\right]\right] \tag{2.14}$$

The velocity distribution can be checked by plotting the line profile. This is obtained by plotting the rate W(z) integrated over z as a function of the detuning Ω_L. However, if the two-photon transition is saturated or if the ionization is too high, this simplified treatment will not be sufficient. The line profile is also dependent on the focal parameters and the detection geometry. All this can be taken into account by solving the rate equations, with the z-dependent two-photon rate, for different detunings and a suffficient number of ellipsoidal shells.

The intensity distribution in the focal volume can be described by a Gaussian beam profile:

$$I(r,z,t) = I_0\left(\frac{S_0}{S_Z}\right) \exp\left[-\delta\left(\frac{r}{r_0}\right)^2 \cdot \left(\frac{t-t_0}{\tau}\right)^2\right] \tag{2.15}$$

With δ being an experimental parameter determining the radial width of the Gaussian distribution. When the laser beam is focused, the focal volume can be described by hyperbolic trajectories of the light beams. We assume cylindrical symmetry and introduce the axis z in the direction of the light propagation with z=0 in the focal plane. The equation of the caustic is then given by

$$\left(\frac{r}{b}\right)^2 - \left(\frac{z}{a}\right)^2 = 1 \tag{2.16}$$

where r represents the distance measured orthogonally to the optical axis z. The parameters a and b are given by the beam divergence θ, the focal length f of the lens and the diameter D of the unfocused laser beam by

$$a = \frac{f^2\theta}{D} \quad \text{and} \quad b = \frac{f\,\theta}{2} \tag{2.17}$$

The isophot surface corresponding to a power density $I_\alpha(r,z,t) = I(t)/\alpha$ can be written as

$$\left(\frac{r}{b}\right)^2 = \frac{1}{\delta}\left(\frac{z^2}{a^2} + 1\right) \ln\left(\frac{q \cdot a^2}{z^2 + a^2}\right) \tag{2.18}$$

For values of α close to one the isophot surfaces approach an ellipsoidal shape with the longitudinal and the transverse half axes equal to

$$a_i = a\sqrt{\alpha - 1} \tag{2.19}$$

$$b_i = b\sqrt{\ln(\alpha)/\delta} \tag{2.20}$$

The volume bounded by an isophot surface corresponding to an attenuation α is given by

$$V_\alpha = \int_0^{z(\alpha)} \frac{2\pi b^2}{\delta}\left(\frac{z^2}{a^2} + 1\right)\ln\left(\frac{\alpha a^2}{z^2+a^2}\right)dz \tag{2.21}$$

After partial integration we obtain:

$$V_\alpha = \frac{2\pi b^2}{\delta a^2}\left[\left(\frac{z^3}{3} + a^2 z\right)\ln\left(\frac{\alpha a^2}{z^2+a^2}\right) + \frac{2z^3}{9} + \frac{4a^2 z}{3} - \frac{4a^3}{3}\arctan(z/a)\right]_0^{z_\alpha} \tag{2.22}$$

If $z(\alpha)$ exceeds limits introduced in the experimental arrangement, e.g. by the use of collimating slits in the atomic beam, the integration may be stopped at an arbitrarily chosen z value.

Isopotential surfaces for some different α values are shown in the figure below. The radius given by an α-value of 1.28 corresponds to one beam waist, the left figure shows isophote curves for α values from 20 to 1.28 and the right from 1.28 to 1.01.

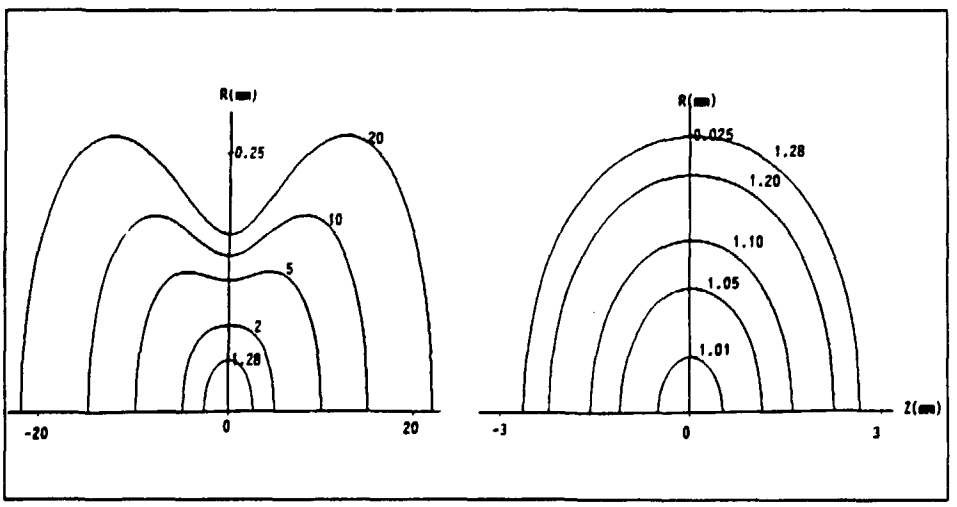

Figure 14. Isopotential surfaces used for calculations on laser excitation rates.

The laser beam is focused using an f=25 cm lens with a beam diameter of 6 mm at the first lens surface.

The fraction of the intensity passing an aperture with a diameter ϕ, corresponding to one beam waist ω_0 (α=1.28), is 86 %. The fraction is given by the relation:

$$I_{trans}/I_{tot} = 1 - \exp(-2\phi^2/\omega_0^2) \qquad (2.23)$$

The alfa value corresponding to N beam waists is given by:

$$\alpha = \exp(N^2/4) \qquad (2.24)$$

Inspection of the isophote surfaces shows that integration out to an attenuation factor of α=20 demands a length of the interaction zone of about 40 mm.

There would be no principal difficulty involved in choosing an arbitrarily detection volume, e.g. square rectangular, if this geometry is preferred in the experiment.

The problem with the velocity spreads for the excitation rates could easily be solved. However, for the Stimulated Emission (SE) rates it is impossible to give a closed expression. This is due to the fact that the SE rates depend on the generated SE itself. The contributions should be obtained by integrating in the frequency, spatial and temporal domain, for each velocity group. The problems arise as we move the resulting SE calculated from a small segment to the neighbouring segments (the progression of the seeding SE). The input parameters are based on exact knowledge of the spectral content of the seeding SE as well as the evolution of the population inversion in the segment. The requirements on the computer are an immense memory as well as enormous speed.

In a cell experiment we have a homogeneous velocity distribution. Therefore, in order to give a general description of the rate equations we now consider CO.

Excitation from the ground state $X\ ^1\Sigma^+$ is made in a two-photon process to the $B\ ^1\Sigma^+$ state. The selection rules for this transition ($\Delta\Lambda$=0) allow ΔJ=0, ±2. In the experiments only the Q-branch was observed (ΔJ=0). With the bandwidth of the laser (0.4 cm^{-1}) a number of rotational lines are excited simultaneously. This is demonstrated in figure 15 showing the Boltzmann distribution in the ground state (15a) and the resulting distribution in the excited state (15b), with the laser frequency centered at the absorption maximum.

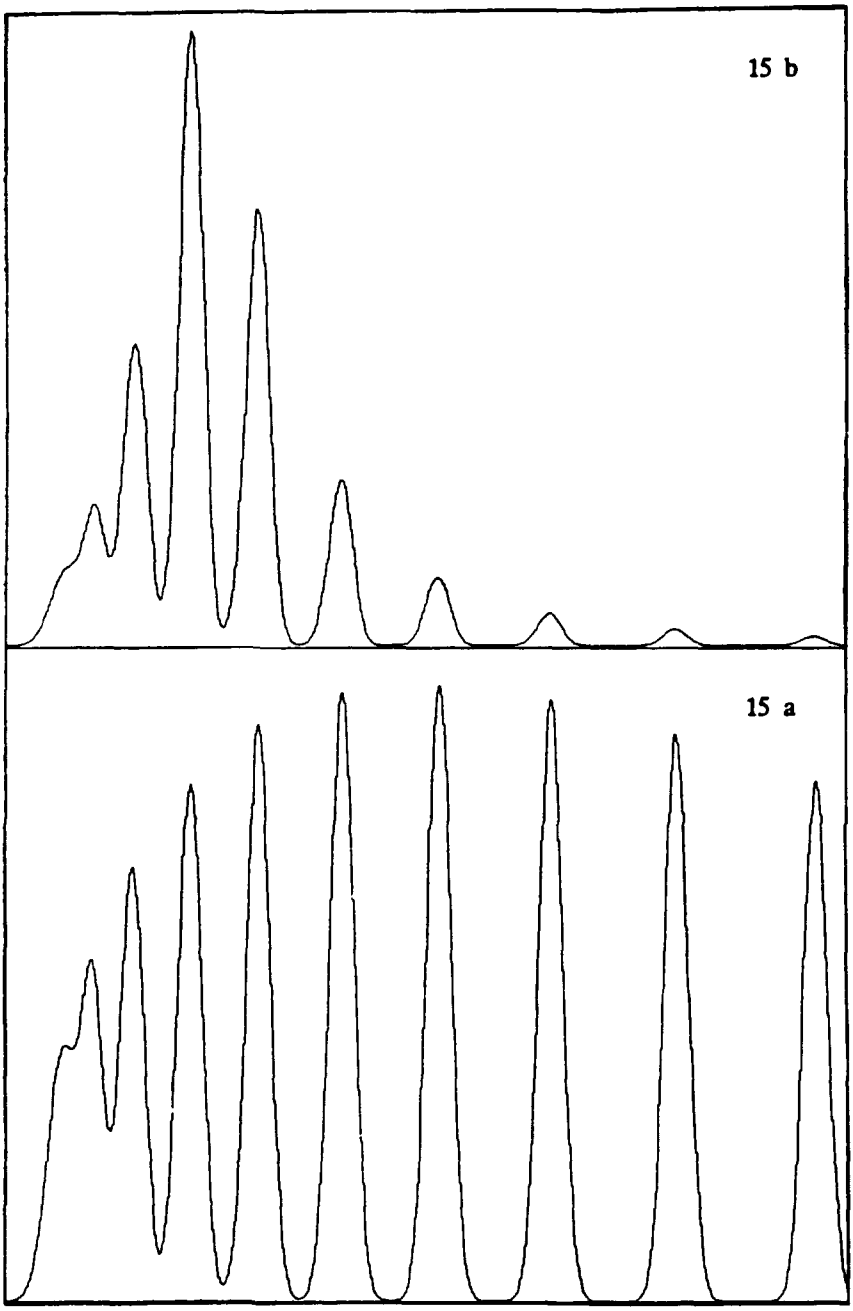

Figure 15. a) The Boltzmann distribution in the ground state of CO at room temperature for J = 0-10. b) The population of the excited B state in CO resulting from two-photon excitation of the ground state.

To include the most dominant levels involved in the excitation process, the rate equations are solved for $v=0$, $J=2$ to $J=6$ of the X state. The fluorescence from the B state to the A $^1\Pi$ state is determined by $\Delta J = 0, \pm 1$.

The linestrengths can be calculated ($\Delta\Lambda=-1$) as

$$\begin{cases} S_P = \dfrac{J+2}{4J+2} \\ S_Q = \dfrac{1}{2} \\ S_R = \dfrac{J-1}{4J+2} \end{cases} \qquad (2.25)$$

Using these Hönl-London factors and the Frank-Condon factors, the decay rates from the B state to the ($v=0$-5, J=1 to J=7) A-states are obtained.Including some extra levels to keep track of the total number of electrons, the rate equations are given by the following expression

$$\begin{cases} \dfrac{dN_1(J)}{dt} = W_{12}(J)\,I^R[N_2(J') - N_1(J)] + \sum_{J'} A_{21}(J')N_2(J') + \sum_{v'',J''} [A_{31}(v'',J'') + P\cdot Q_{31}(v'')]N_3(v'',J'') \\ \dfrac{dN_2(J')}{dt} = W_{12}(J)I^R[N_1(J) - N_2(J')] - [W_{2I}I + A_2(J') + P\cdot Q_2(J')]N_2(J') - \sum_{v'',J''} F_{v'',J''}B_{23}(v'',J'')[N_2(J') - \dfrac{2J''+1}{2J''+1}N_3(v'',J'')] \\ \dfrac{dN_3(v'',J'')}{dt} = \sum_{J'} F_{J''}B_{23}(J')[N_2(J') - \dfrac{2J''+1}{2J''+1}N_3(v'',J'')] + \sum_{J'} A_{23}(J')N_2(J') - [A_3(v'',J'') + P\cdot Q_3(v'',J'')]N_3(v'',J'') \\ \dfrac{dN_4}{dt} = \sum_{J'} A_{24}(J')N_2(J') + \sum_{v'',J''} [A_{34}(v'',J'') + P\cdot Q_{34}(v'',J'')]N_3(v'',J'') \end{cases}$$

The set of equations for the populations $N_i(v,J)$ are described in detail in paper 10, however, the dependence on v and J are governed by the type of arguments given above, e.g. for the Hönl-London factors. If the seed for the SE is assumed to start from spontaneously emitted photons, the calculation of the SE is straightforward. The contribution to the SE is shown in figure 16.

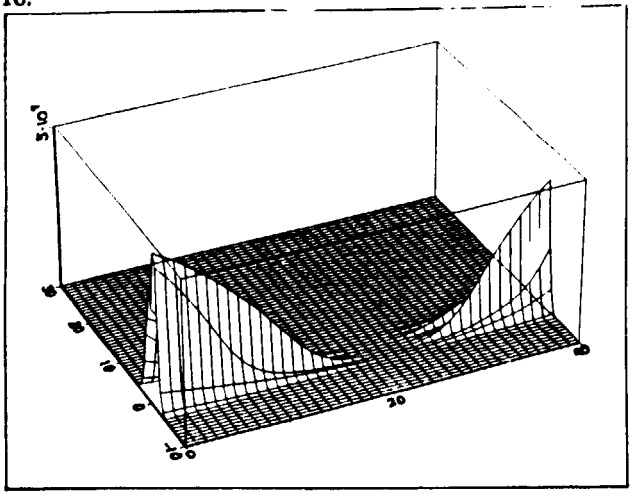

Figure 16. The z-axis displays the relative number of stimulated emission photons originating from the specific segment. The distance along the laser beam is the x-axis and the cell length was 40 cm. The time runs in the y-direction for a period of 40 ns.

3. Beam deflection electron density measurements

The following discussion serves as an introduction by using simplified arguments to describe the principles of the beam deflection technique. As a laser-produced plasma expands in a vacuum chamber the electron density decreases with increasing distance $\bar{r}$ from the target. If the electron density is lower than a critical value n_c, we can give an approximate expression for the index of refraction of free electrons

$$n = 1 - n_e/2n_c \qquad (3.1)$$

With the critical electron density defined as

$$n_c = \epsilon_o m_e \left(\frac{\omega}{e}\right)^2 \approx 2.5 \cdot 10^{21} cm^{-3} \qquad (3.2)$$

the value given corresponds to the density resulting in total reflection of a HeNe laser beam. If a laser beam is sent through the plasma the varying density will deflect the beam. This deflection is approximately described by

$$\alpha(y) = \frac{1}{n_0} \int \frac{dn}{dy}\, dx \qquad (3.3)$$

By measuring deflection angles at different distances from the target and assuming a spherically symmetric plasma, the electron density in the plasma can be calculated using a tomographic technique [3.1].

A description of the tomographic procedure [3.2] will be given below. However, as the procedure differs for a deflection measurement compared to a normal absorption measurement, we start with the normal case.

As indicated in figure 17 the projection of a distribution f(x,y) can be calculated as

$$p(y',\theta) = \int_{-\infty}^{\infty} f(x',y')\, dx' \qquad (3.4)$$

where a rotation of the y-axis an angle of θ yields: $y' = y\cos\theta - x\sin\theta$.

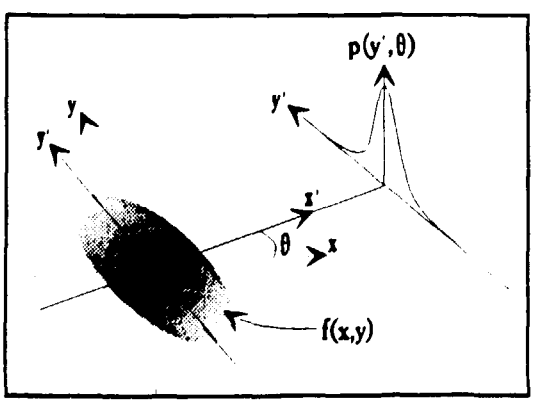

Figure 17. The different parameters used in the tomographic calculation of the electron density using the beam deflection technique.

After some manipulation the function f(x,y) can be reconstructed from the so called convolution backprojection integral

$$f(x,y) = \int_0^{\pi} p(y',\theta) \circledast k1(y')\, d\theta \qquad (3.5)$$

The function k1(y') shown in figure 18 is the inverse transform of a filter function used in the frequency domain. If this is applied to the beam deflection technique in a medium with an index of refraction described by

$$n(\bar{r}) = n_0[1 + \hat{n}(\bar{r})] \qquad (3.6)$$

where $\hat{n}(\bar{r})$ is a localized normalized variation of the index of refraction, the deflections are given by

$$\alpha(y',\theta) \approx \frac{d}{dy'} \int \hat{n}(x',y')\, dx' \qquad (3.7)$$

Using this "transverse gradient projection" with

$$p(y',\theta) = \int \hat{n}(x',y')\, dx' \qquad (3.8)$$

we can find a similar convolution back-projection integral for the index variations as

$$\hat{n}(x,y) = \int_0^{\pi} \alpha(y',\theta) \circledast k2(y')\, d\theta \qquad (3.9)$$

The filter function will be different in this case and is shown in figure 18 together with the function for a normal absorption measurement.

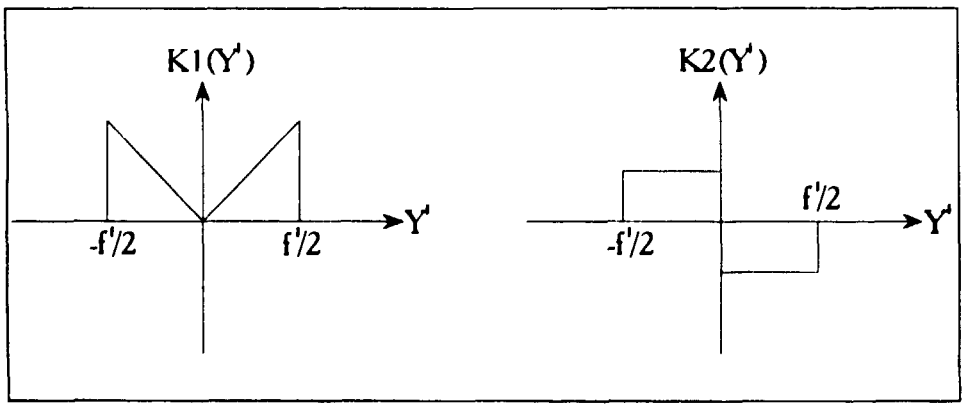

Figure 18. Two filter functions used in tomographic reconstruction procedures.

4. Light in flight

Light-in-Flight Holography, LIFH, is a method for producing a continuous frameless 3D film which records at a velocity higher than or equal to the velocity of light [4.1]. The interference fringes can be formed on a holographic plate only when the difference in the time of flight for the object and the reference light is less than the limit imposed by the coherence length.

In normal LIFH the exposure time is determined by the velocity with which the reference beam intersects the plate. This can be compared to a camera with a curtain shutter which moves along the film. The motion of the shutter over the film results in a time difference between the left and the right end of the film corresponding to the shutter speed times the length of the frame. This implies that a time scale can be assigned to the film.

Assuming a reference pulse with the wavefront perpendicular to the light ray and a width τ crossing the plate with an angle θ to the normal, we get the exposure time t_N over a plate with length L

$$t_N = \frac{L}{v} = \frac{L \cdot \sin\theta}{c} \approx 0.8 \text{ ns} \qquad (4.1)$$

With a Gaussian temporal profile the slit width w_N is

$$w_N = \sqrt{2}\,\frac{c\tau}{\sin\theta} \approx 4.5 \text{ mm} \qquad (4.2)$$

the values are typical for the parameters used in the experiments τ = 10 ps, L = 25 cm and $\theta = 70^{\circ}$.

It is obvious that by decreasing θ, the shutter approaches infinite velocity. The motivation for the experiments with the expanded view time is that it is often interesting to study processes of longer duration.

The following trivial solutions have been suggested for expanding the exposure time: increasing θ to 90°, prolonging the plate length or diminishing c by using a media with a high refractive index. In paper 13 a technique with skew reference pulses is described and in [4.2] the use of multiple reference pulses is described. These two techniques will be discussed below.

The experimental arrangements for both techniques are shown in figure 19.

The first technique exploits the fact that the diffraction off a grating results in a pulse with the pulse front leaning towards the light ray. In the following discussion we neglect the pulse width as well as the pulse dispersion after diffraction.

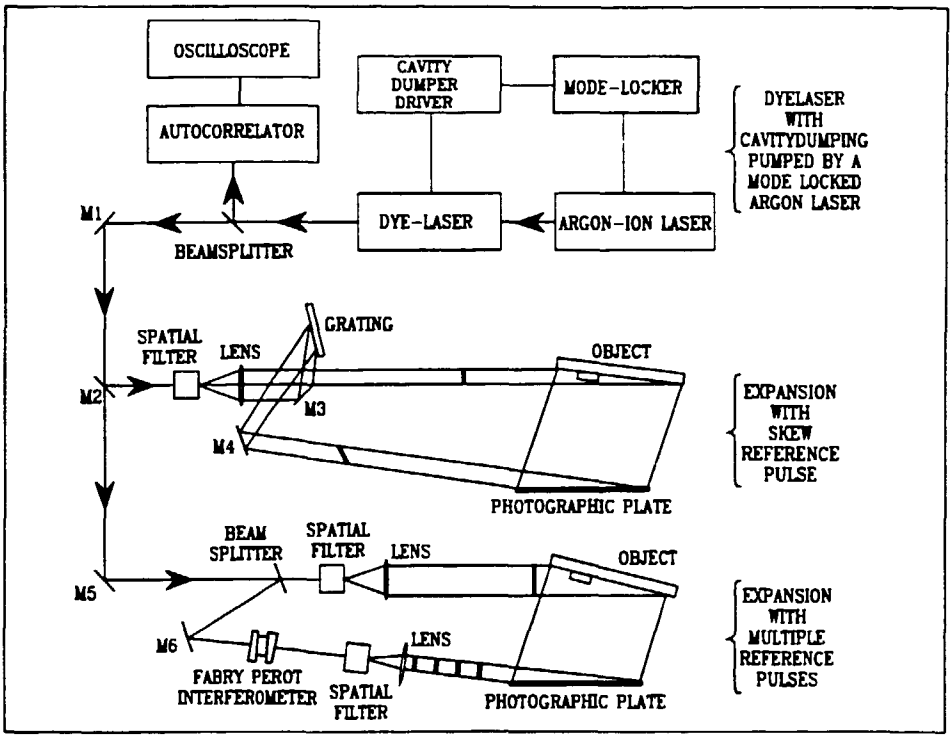

Figure 19. The experimental arrangements for light in flight holography. The illumination of the upper plate results in an expansion of the view time due to the skew reference pulse, whereas the expansion on the lower plate is due to multiple reference pulses.

If we introduce the relative shutter speed R = v/c with a normal pulse having the pulse front perpendicular to the light ray we get

$$R_N = \frac{1}{\sin\theta} \qquad (4.3)$$

with θ being the angle of incidence on the photographic plate as before.

If we assume that the pulse front is leaning "a skew reference pulse" with an angle β which is zero in the normal, perpendicular case, we get a relative shutter speed of

$$R_S = \frac{\cos\beta}{\sin(\theta+\beta)} \qquad (4.4)$$

which is the same as equation 4.3 for $\beta = 0$. As described in paper 13, a tilt angle of 70^o can easily be obtained. The resulting view time expansion was given by the factor $E = t_S/t_N$. This is, however, not an appropriate description since the angle of incidence can be optimized for a certain angle of skewness. A better way to describe the increase in view time is probably the use of a shutter speed relative to the speed of light.

This will be outlined in the following by some simplified geometrical assumptions. Since it is no problem to obtain a tilt angle of $\beta = 45^{o}$ this will be used in the following. In this case an arrangement with a number of prisms and two gratings can be used for multiple diffractions. A simplified schematic of this is shown in figure 20.

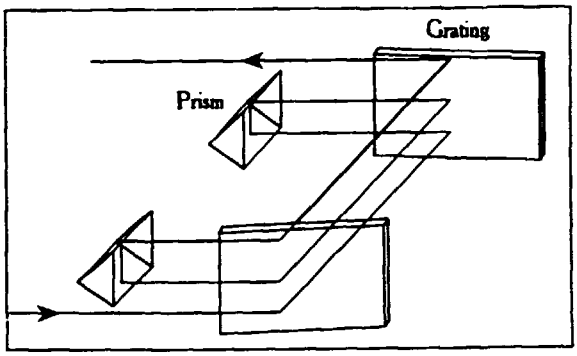

Figure 20. An arrangement for increasing the tilt angle of the reference pulse using multiple diffractions in a grating pair.

This setup, with the gratings in grazing incidence, results in an angle β given by the relation

$$\tan\beta = n \tag{4.5}$$

after diffraction in the gratings n times. This gives a velocity reduction of

$$R_S = \frac{1}{\sin\theta + n \cdot \cos\theta} \tag{4.6}$$

Differentiating this gives the optimal angle of incidence as

$$\theta_{opt} = \arctan(1/n) \tag{4.7}$$

After some manipulation we arrive at the optimal velocity reduction

$$R_S^{opt} = (1 + n^2)^{-1/2} \tag{4.8}$$

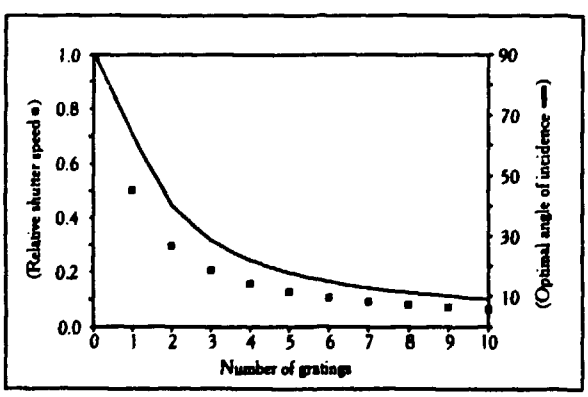

Figure 21. A plot of the slowing down of the shutter speed (squares) as a function of the number of used gratings. The angle of incidence (solid line) giving optimal view time expansion as well as the shutter speed are obtained assuming a tilt of 45° in each grating.

The technique with the multiple reference pulses, also shown in figure 19, speaks for itself. In figure 22 a photo of the object and of the resulting hologram, is shown for illustration. The viewtime expansion is determined by the separation in the interferometer and by the number of pulses visible on the holographic plate. The main advantage with this train of reference pulses was, however, not the viewtime expansion but the possibilities to examine geometrical distortions from a single point of observation, instead of trying to evaluate the change in pulse form by moving along the plate. Another advantage is the exact time scale given by the separation of the pulses which can be used directly in the hologram. This is further discussed in [4.2].

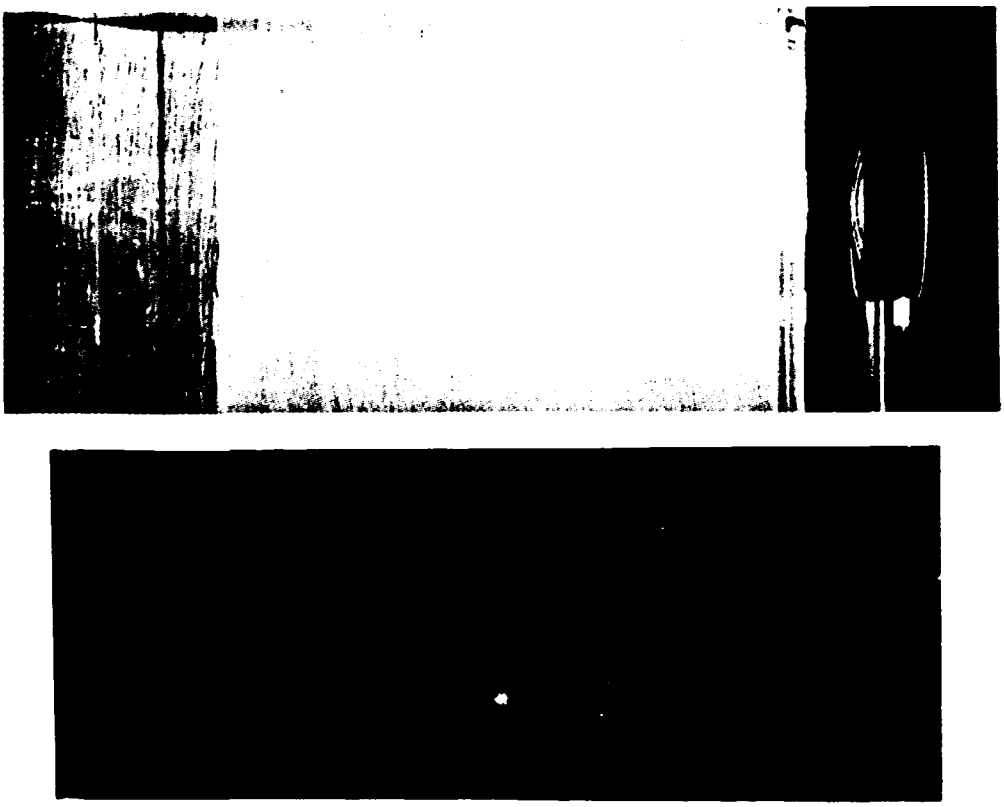

Figure 22. a) The experimental arrangement used for LIFH of the focusing of a short pulse in a scattering medium. b) A photograph of the resulting hologram. The spherical apperance of the laser pulse is due to a geometrical distortion resulting from the fact that different points in space are recorded at different points in time.

5. Comments on the papers.

The papers have been arranged so that the first six papers deal with lifetime measurements.
Paper 6, 7 and 8 are concerned with hyperfine structure measurements.
Paper 9 and 10 deal with the measurements of two-photon and ionization rates together with investigations on stimulated emission.
Paper 11 treats electron density measurements in the laser-produced plasma utilized in paper 5, 6 and 9.
Finally, paper 12 and 13 treat light-in-flight holography.

The papers are the results of extensive team work both within the department and with people outside the department as well as outside the field of atomic physics.
My contribution to these papers have been mainly in the experimental part. However, in the following chronological discussion I will point out where I have taken part in any theoretical work.

The first two papers I took part in are paper 1 and 2. After this I was involved in a project that was initiated by W. Schade from Kiel where an effusive hollow cathode had been developed. This was later further developed and resulted in four publications, paper 3, 4, 7 and 8. Regarding paper 4 that deal with determination of the solar abundance of gadolinium it should be pointed out that the solar analysis was performed by prof. E. Biémont in Liège whereas we performed the measurements on the transition probabilities at our department. The calculations of lifetimes in silicon in paper 5 were performed by all authors as a case study for getting acquainted with the MCHF program-package developed by C. Froese-Fisher.
During the experiments on carbon in paper 9 some calculations on ASE were initiated which later resulted in the publication of paper 10 with more extensive calculations using the rate-equation approach.

6. Acknowledgements

I want to thank:
my supervisor Hans Lundberg for not only being the supervisor you expect in the common sence, but also a co-worker. You taught me the most important part of research, to always pursue quality rather than quantity which, to my surprise, you were able to do even late at night.
Anders Persson who taught me the importance of always having a "hög imponans grad", i.e. a lot of computer controlled electronic devises with lots of led's. This could only be replaced by a juicy steak at the best resturant in town.
Sune Svanberg for enticing me into the field of atomic physics as well as for establishing the monetary means needed for the different projects.
Stefan Kröll for the many stimulating discussions on physics in general.
all my co-authors and friends at the department who have helped me throughout my PhD.
Sara, all I can say to you is that I will always love you.

7. References

1.1 D.M.Brink and G.R.Satchler, Angular Momentum, Clarendon Press (1961)

1.2 M.Weissbluth, Atoms and Molecules, Academic Press (1978)

1.3 I.Lindgren and A.Rosén, Case Stud.At.Phys.4, 93 (1974)

1.4 C.Froese Fischer, DOE Report No. DOE/ER/10618-11 (1983)

1.5 K.Blum, "Density matrix formalism and spectroscopy", 73-109, Progress in Atomic Physics

1.6. W.Demtröder, Laser Spectroscopy, Springer-Verlag (1988)

2.1 J.Brossel and F.Bitter, Phys.Rev.86, 308 (1952)

2.2 T.W. Hänsch, M.D.Levenson and A.L.Schawlow, Phys.Rev.Lett.26, 946 (1971)

2.3 M.S.Sorem and A.L.Schawlow, Opt.Comm.5, 148 (1972)

2.4 S.C.Wieman and T.W. Hänsch, Phys.Rev.Lett.36, 1170 (1976)

2.5 J.E.Lawler, A.I.Ferguson, J.E.M.Goldsmith, D.J.Jackson and A.L.Schawlow, Phys.Rev.Lett.42, 1046 (1979)

2.6 G.C.Bjorklund, Opt.Lett.5, 15 (1980)

2.7. T.W.Hänsch, D.R.Lyons, A.L.Schawlow, A.Siegel, Z.-Y.Wang and G.-Y.Yan, Opt.Comm.38, 47 (1981)

2.8 S.Svanberg, G.-Y.Yan, T.P.Duffey and A.L.Schawlow, Opt.Lett.11, 138 (1986)

2.9 R.A.McFarlane, W.R.Bennet and W.E.Lamb, Appl.Phys.Lett.2, 189 (1963)

2.10 W.E.Lamb, Phys.Rev.134A, 1429 (1964)

2.11 V.S.Lethokov and V.P.Chebotayev, Nonlinear Laserspectroscopy, Springer-Verlag Berlin (1977)

2.12 J.L.Hall, T.Bear, L.Hollberg and H.G.Robinson, Laser Spectroscopy V, Springer-Verlag Berlin (1981)

2.13 R.E.Imhof and F.H.Read, Rep.Prog.Phys.40, 1 (1977)

2.14 J.Carlsson nad L.Sturesson, Z.Pys.D 14, 281 (1989)

2.15 A.Gaupp, P.Kuske and H.J.Andrä, Phys.Rev.A 26, 3351 (1982)

2.16 J.K.Link, J.Opt.Soc.Am.56, 1195 (1966)

2.17 D.V.O'Connor and D.Phillips, Time-correlated Single Photon Counting, Academic Press (1984)

2.18 A.Persson, Doctoral Dissertation, Lund Reports on Atomic Physics LRAP-116, Dept. of Physics Lund Inst. of Technology (1990)

2.19 C. Kittel, H. Kroemer, Thermal Physics, 2nd ed. W. H. Freeman and Company, San Francisco (1980)

2.20 N.F.Ramsey, Molecular Beams, Oxford Univ. Press, London (1956)
2.21 C.R.Vidal and F.B.Haller, Rev.of Sci.Instr.**42**, 1779 (1971)
2.22 S.Büttgenbach, Springer tracts in modern Physics **96** (1982)
2.23 M.E.Pillow, Spect. Acta **36B**, 821 (1981)
2.24 N.Laegreid and G.K.Wehner, J.Appl.Phys.**32**, 365 (1961)
2.25 S.Kröll and A.Persson, Opt.Commun.**54**, 277 (1985)
2.26 D.W.Duquette, S.Salih and J.E.Lawler, Phys.Lett.**83A**, 214 (1981)
2.27 B.C.Boland, F.E.Irons and R.W.P.Mc.Wirther, J.Phys.B **1**, 1180 (1968)
2.28 P.K.Carroll and E.T.Kennedy, Contemp.Phys.**22**, 61 (1981)
2.29 H.Bergström and H.Lundberg, Proceeding from the 11'th EGAS Conf.Uppsala (1990)
2.30 A.C.Eckbreth, Laser Diagnostics for Combustion and Species, Abacus press, (1988)
2.31 T.H.Maiman, Nature,**187**, 493 (1960)
2.32 P.P.Sorokin and J.R.Lankard, IBM J.Res.Develop.**10** (1966)
2.33 O.G.Peterson, S.A.Tuccio and B.B.Snavely, Appl.Phys.Lett.**17**, 245 (1970)
2.34 Y.R.Shen, The Principles of Nonlinear Optics, Wiley (1984)
2.35 S.Haroche, Topics in Appl.Phys.Vol **13**, Ed. K.Shimoda, Springer Verlag
2.36 W.K.Bischel, B.E.Perry and D.R.Crosley, Appl.Opt.**21**, 1419 (1982)

3.1 G.W.Faris and R.L.Byer, Appl.Opt.**27**, 5202 (1988)
3.2 R.N.Bracwell and A.C.Riddle, Astrophys.J.**150**, 427 (1967)

4.1 N.Abramson, Appl.Opt.**22**, 215 (1983)
4.2 S.G.Petterson, H.Bergström and N.Abramson, Proceedings of the International Symposium on Display Holography, Vol III, 315, Lake Forest Illinois (1988)